Nature Communications

https://doi.org/10.1038/s41467-026-74288-2

Article in Press

Ionic self-assembled monolayers enable neutral interfaces and synergistic charge extraction in high-efficiency perovskite solar cells

Received: 18 November 2025

Accepted: 3 June 2026

Cite this article as: Yang, Y., Krisiune, D., Xu, Y. *et al.* Ionic self-assembled monolayers enable neutral interfaces and synergistic charge extraction in high-efficiency perovskite solar cells. *Nat Commun* (2026). https://doi.org/10.1038/s41467-026-74288-2

Yuxuan Yang, Deimante Krisiune, Yuliang Xu, Xuehui Liu, Qiangqiang Zhao, Yongde Xu, Hao Tian, Ernestas Kasparavicius, Zhiyu Gao, Xu Fu, Bao Zhang, Jianxing Xia, Chuanxiao Xiao, Shuping Pang, Vytautas Getautis, Dewei Zhao, Kasparas Rakstys & Yi Zhang

Ionic Self-Assembled Monolayers Enable Neutral Interfaces and Synergistic Charge Extraction in High-Efficiency Perovskite Solar Cells

Yuxuan Yang[1#], Deimante Krisiune[2#], Yuliang Xu[3#], Xuehui Liu[4], Qiangqiang Zhao[5], Yongde Xu[1], Hao Tian[6], Ernestas Kasparavicius[2], Zhiyu Gao[3], Xu Fu[7], Bao Zhang[7], Jianxing Xia[1], Chuanxiao Xiao[6,8], Shuping Pang[5], Vytautas Getautis[2], Dewei Zhao[3,*], Kasparas Rakstys[2,*], Yi Zhang[1,*]

# Yuxuan Yang, Deimante Krisiune and Yuliang Xu contributed equally.

[1] Institute of Molecular Plus, School of Chemical Engineering and Technology, Tianjin University, Tianjin 300072, China

[2] Department of Organic Chemistry, Kaunas University of Technology, Radvilenu pl. 19, Kaunas 50254, Lithuania

[3] College of Materials Science and Engineering and Engineering Research Center of Alternative Energy Materials and Devices, Ministry of Education, Sichuan University, Chengdu 610065, China.

[4] School of Energy and Chemical Engineering, Tianjin Renai College, Tianjin 301636, China

[5] State Key Laboratory of Photoelectric Conversion and Utilization of Solar Energy, Qingdao Institute of Bioenergy and Bioprocess Technology, Chinese Academy of Sciences, Qingdao 266101, China

[6] Ningbo Institute of Materials Technology and Engineering, Chinese Academy of Sciences, Ningbo 315201, China

[7] School of Chemical Engineering and Technology, Tianjin University, Tianjin 300350, China

[8] Ningbo New Materials Testing and Evaluation Center Co., Ltd, Ningbo 315201, China

Emails: dewei_zhao@hotmail.com; kasparas.rakstys@ktu.lt; yi_zhang@tju.edu.cn

Abstract

Self-assembled monolayers (SAMs) have become indispensable hole-selective contacts for high-efficiency inverted perovskite solar cells (PSCs). However, the intrinsically acidic head groups of conventional SAMs lead to interfacial inhomogeneity, limited charge transfer, and poor operational stability. Here, we introduce a family of alkali metal–based phosphonate salts (2PACz-M) through targeted head-group functionalization of the benchmark [2-(9H-carbazol-9-yl)ethyl]phosphonic acid (2PACz) SAM, achieving a chemically neutralized and electronically delocalized interface. The ionic phosphonate moiety enhances π-electron conjugation, improves energy-level alignment, and strengthens chemical coordination with metal oxide electrodes, resulting in homogeneous and stable surface coverage. Moreover, when combined with [4-(3,6-dimethyl-9H-carbazol-9-yl)butyl]phosphonic acid (Me-4PACz), the mixed-SAM interface exhibits a synergistic effect that facilitates efficient hole extraction, suppresses non-radiative recombination, and reinforces environmental robustness. This interfacial engineering enables 1.55 eV PSCs to achieve a champion power conversion efficiency (PCE) of 26.88% with a fill factor (FF) of 86.57%, alongside a 23.32% PCE for a 29.7 cm^2 module. The SAM synergy proves universal across perovskites of varied bandgaps, yielding two-terminal (2T) all-perovskite tandem solar cells with an enhanced PCE of 29.05%.

Introduction

Metal halide perovskites (PVKs) have attracted widespread attention owing to their outstanding light-harvesting ability, efficient charge transport, and tunable bandgaps[1,2]. Perovskite solar cells (PSCs) and modules have demonstrated remarkable commercial potential, achieving high power conversion efficiencies (PCEs) at low fabrication costs[3-8]. Among the diverse device architectures, inverted (p–i–n) PSCs have rapidly advanced with the introduction of self-assembled monolayers (SAMs) as hole transport layers (HTLs). SAMs offer several advantages, including adjustable energy levels, strong substrate anchoring, and reduced interfacial energy loss. Consequently, a wide range of SAMs with innovative chemical structures have been developed and implemented in perovskite photovoltaics in recent years[9-12].

Structurally, SAMs typically consist of three segments: a functional group, a spacer, and an anchoring group. The anchoring group covalently binds SAMs to metal oxide substrates (e.g., transparent conductive oxide, TCO, or nickel oxide, NiO_x), with carboxylic and phosphonic acids being the most common choices[13-17]. However, these traditional anchoring groups often lead to insufficient dipole moments, acid-induced substrate corrosion, and dependence on organic solvents. To address these limitations, several design strategies have been explored. π-Conjugated benzene rings or donor–π–acceptor (D–π–A) structures have been incorporated into [2-(9H-carbazol-9-yl)alkyl]phosphonic acid (PACz) molecules to yield derivatives such as (4-(7H-dibenzo[c,g]carbazol-7-yl)butyl)phosphonic acid (4PADCB) and 4-(7-(4-(bis(4-methoxyphenyl)amino)-2,5-difluorophenyl) benzo[c][1,2,5]thiadiazol-4-yl) benzoic acid (PAFTB)[18-20], thereby enhancing dipole moments and interfacial binding[20]. Meanwhile, milder boric acid groups, such as in (4-(di-p-tolylamino)phenyl)boronic acid (MTPA-BA) and 4-dibenzothienyl boronic acid (S-BA), effectively suppress substrate corrosion[21,22]. Amphiphilic molecules, including (2-(4-(bis(4-methoxyphenyl)amino)phenyl)-1-cyanovinyl)phosphonic acid (MPA-CPA) and (1-cyano-2-(10-(4-methoxyphenyl)-10H-phenoxazin-3-yl)vinyl)phosphonic acid (RS-2), featuring hydrophilic cyanovinyl phosphonic acid fragments of different polarity, have also been introduced[1,23]. Nevertheless, π-extension increases dipole moments by only a few

Debyes—insufficient for strong interfacial dipole formation, while boric acid anchoring can lead to energy-level mismatch[22]. Furthermore, weak acidic SAMs remain corrosive under harsh conditions, and amphiphilic SAMs pose synthetic challenges due to micelle formation. Moreover, almost all current SAMs exhibit limited water solubility, posing challenges to the operational practicality and environmental friendliness required for the industrial compatibility and commercialization of PSCs.

Beyond these individual modifications, different SAMs with distinct characteristics can work synergistically in PSCs, serving as both chemical and electronic bridges between the perovskite and the substrate. Although the pioneering [2-(9H-carbazol-9-yl)ethyl]phosphonic acid (2PACz) and [4-(3,6-dimethyl-9H-carbazol-9-yl)butyl]phosphonic acid (Me-4PACz) families maintain high device efficiencies, they still exhibit intrinsic drawbacks[24,25]. To overcome such issues, mixed-SAMs strategies have been developed to mitigate non-wetting and aggregation problems[26,27], achieving fully covered and uniform HTLs[28,29], improved interfacial bonding[30,31], optimized energy alignment, and defect passivation[32,33]. Despite these advances, most approaches address only isolated aspects of the problem. Therefore, a rational molecular design that can synergistically overcome the inherent weaknesses of current SAMs remains essential.

In this work, we employ a simple neutralization strategy to synthesize alkali-metal phosphonate salt SAMs (2PACz-M, where M = Li, Na, K, Rb, or Cs), representing, to the best of our knowledge, the first demonstration of SAM formation from salt solutions. The ionic nature of 2PACz-M enhances solubility in polar green solvents such as water, while the increased hydrophilicity of the resulting SAM layer improves compatibility with perovskite inks. Both theoretical calculations and experiments reveal that potassium (2-(9H-carbazol-9-yl)ethyl)phosphonate (2PACz-K) exhibits an exceptionally large dipole moment and enhanced π-electron delocalization, leading to efficient hole extraction, defect suppression, and superior stability. The neutralized, non-acidic phosphonate head group also prevents the acid-induced corrosion of indium tin oxide (ITO) and NiO_x. Devices based on 2PACz-K achieve a PCE of 25.56%, outperforming those based on 2PACz (24.07%). Furthermore, a mixed-SAM strategy

combining Me-4PACz and 2PACz-K yields superior interfacial contact, effective hole transfer, and well-aligned energy levels, resulting in enhanced device stability. Consequently, 1.55 eV small-area devices reach a champion PCE of 26.88% with an ultra-high FF of 86.57%, while a 29.7 cm^2 module achieves a remarkable PCE of 23.32%. The universality of this SAM synergy strategy is further validated across various SAMs and perovskite compositions, and 2T all-perovskite tandem solar cells deliver an impressive PCE of 29.05%.

Results and Discussion

Molecular characteristics of 2PACz and 2PACz-M

The head functionalization strategy was applied to 2PACz to develop 2PACz-M salts, where M represents Li, Na, K, Rb, or Cs (chemical structures shown in Fig. 1a). These compounds were directly synthesized through a straightforward acid–base neutralization reaction (Supplementary Methods, Supplementary Fig. 1). To elucidate the molecular characteristics of the SAMs, we performed density functional theory (DFT) calculations by Gaussian and ORCA and wavefunction analyses with the Multiwfn code[34,35]. The 2PACz-M SAMs exhibit markedly enhanced dipole moments (μ) compared with 2PACz (Fig. 1b), among which 2PACz-K shows the largest μ value of 13.27 D (Supplementary Fig. 2-3), in agreement with atomic dipole–corrected Hirshfeld (ADCH) and Mulliken charge analyses (Supplementary Fig. 3)[36]. Electrostatic potential (ESP) maps reveal positively charged alkali-metal cations and negatively charged carbazole phosphonate fragments (Fig. 1c, Supplementary Fig. 4-5). Based on the ESP extrema and spatial distribution (Fig. 1d, Supplementary Fig. 6-7), 2PACz-K displays an increased ESP difference ($\Delta\varphi$) and a higher molecular polarity index (MPI), resulting in a larger polar surface area[37]. This pronounced charge separation and polarity generate a strong interfacial electric field[20], which modulates the energy level alignment, enhances hole extraction[38], and strengthens binding interactions with both perovskite and substrate.

Average local ionization energy (ALIE) was further used to describe electron reactivity within the molecules[39,40]. As shown in Fig. 1e and Supplementary Fig. 8-9, 2PACz-K exhibits lower ALIE

values around the carbazole ring compared with 2PACz, indicating that electrons in this region are more weakly bound—consistent with the negatively charged ESP regions. Similarly, photoelectron spectroscopy in air (PESA) and orbital-weighted dual descriptor analyses (Supplementary Fig. 10-11) confirmed the superior electron-donating ability of 2PACz-K[41]. These highly delocalized π-electrons can interact strongly with under-coordinated Pb^{2+} ions at the buried perovskite interface through Lewis acid–base interactions, as verified by NMR spectra (Supplementary Fig. 12), thereby suppressing interfacial defects. Independent gradient model based on Hirshfeld partition of molecular density (IGMH), interaction region indicator (IRI), topology analyses based on the atoms-in-molecules (AIM) theory and *ab-initio* molecular dynamics (AIMD) simulations further confirmed the interaction between 2PACz-K and PbI_2 (Fig. 1f, Supplementary Fig. 13-16)[42-44]. Based on charge decomposition analysis (CDA), 0.14 electron transfers from 2PACz-K to PbI_2 (Fig. 1g), with the binding energy of -0.975 eV. Furthermore, the electron transfer characteristics of SAMs were explored through IGMH and charge density difference (CDD) in Fig. 1h-j. 2PACz-K transfers more electron to perovskite and ITO than 2PACz (Supplementary Fig. 17-18), consistent with ALIE and ESP analyses.

Unlike the covalent O–H bonds in 2PACz, ionic O–K bonds were identified in 2PACz-K, as evidenced by Laplacian of electron density, valence electron density maps, electron localization function (ELF) and localized orbital locator (LOL)[43]. Specifically, Fig. 1k and Supplementary Fig. 19 show pronounced electron sharing between O and H atoms in 2PACz, whereas the negligible electron localization between O and K atoms in 2PACz-K is characteristic of non-covalent ionic interactions. The ionic nature of these O–K bonds was further confirmed by IRI and IGMH results (Supplementary Fig. 20). The relatively dissociated O–K bonds facilitate the formation of stable P–O–Ni linkages, thereby ensuring intimate interfacial contact between 2PACz-K and NiO_x[45]. Notably, density-of-states (DOS) analyses indicate that the phosphonate group in 2PACz-K contributes to both the highest occupied molecular orbital (HOMO) and lowest unoccupied molecular orbital (LUMO) (Supplementary Fig. 21). Owing to the replacement of ionizable H with K atoms, 2PACz-K exhibits a non-acidic character, effectively mitigating the corrosion of ITO and

NiO_x (Supplementary Fig. 22-23) and improving the interfacial stability of PSCs.

In addition, the solubility behavior of 2PACz-K and the benchmark SAM Me-4PACz was investigated by classical molecular dynamics (MD) simulations[46,47]. The periphery of the solvent clusters is outlined by a translucent sphere for easy observation. As illustrated in Fig. 1m-n, Supplementary Fig. 24 and Supplementary Movies 1-2, Me-4PACz molecules are excluded out of water clusters, indicating the negligible solubility in water. While 2PACz-K molecules disperse well in water with larger solvent accessible surface area (SASA), suggesting 2PACz-K is soluble in water. Besides, Me-4PACz molecules tend to aggregate in ethanol (EtOH) solution, while adding 2PACz-K avoids the aggregation of Me-4PACz (Fig. 1o-p, Supplementary Fig. 25, Supplementary Movies 3-4). Dissolution tests corroborate these predictions (Supplementary Fig. 26). Using aqueous 2PACz-M solutions to form SAM layers yields uniform perovskite films with high quality (Supplementary Fig. 27-30). Specifically, the perovskite films on 2PACz-(Na, K, Rb, Cs) are more uniform and compact with larger grain size than that on 2PACz-Li. The resulting device based on 2PACz-K achieved a PCE of 25.37% and an FF of 84.56% (Supplementary Fig. 31). Furthermore, ethanol solutions of 2PACz-M exhibit high optical transparency in the visible range, minimizing light loss in PSCs (Supplementary Fig. 32-33). When dissolved in EtOH/DMF (10:1 v/v), the 2PACz-K–based device achieved a champion PCE of 25.56%, outperforming its 2PACz counterpart (24.07%) (Fig. 1l, Supplementary Table 1), highlighting the effectiveness of this head-functionalization strategy for SAM engineering.

Interactions between SAMs and perovskite

Regarded as one of the most representative SAMs for perovskite photovoltaics[48,49], Me-4PACz still suffers from deficient interfacial quality, limited charge transfer, and unsatisfactory stability[24-33]. Here, we design a synergistic SAM system combining Me-4PACz and 2PACz-M (denoted as Me+M) to integrate their respective advantages.

We first investigated the intermolecular interaction between Me-4PACz and 2PACz-K. Van der Waals (vdW) potential, ESP, and ALIE analyses reveal that the electron-rich carbazole moieties

dominate the π–π interaction between SAMs (Fig. 1c, Fig. 1e, Supplementary Fig. 34-35). The green isosurfaces in the IGMH maps further visualize these π–π interactions (Fig. 2a, Supplementary Fig. 36), which are corroborated by energy decomposition, IRI, IRI-π, electron density topological analyses and AIMD simulation (Supplementary Fig. 36-40). In addition, ^{1}H-NMR spectra show clear chemical-shift variations of aromatic protons upon mixing Me-4PACz and 2PACz-K (Supplementary Fig. 41), confirming the existence of π–π interactions.

The surface quality of the SAM layers was then examined. Contact-angle measurements using DMF and DMSO droplets indicate that Me-4PACz exhibits poor wettability toward perovskite precursor solutions due to its hydrophobic nature (Supplementary Fig. 42), which can result in low film coverage. In contrast, incorporating 2PACz-M mitigates this nonwetting behavior, yielding more uniform perovskite coverage (Supplementary Fig. 42-44). SEM-EDX mapping, photographs and *J–V* characteristics further reveal that Me-4PACz forms aggregated domains and uncovered regions (Supplementary Fig. 45-46), whereas the Me+K mixture produces a denser and more uniform distribution whether NiO_x exists or not, likely due to ordered molecular packing facilitated by π–π interactions.

The anchoring strength of SAMs on NiO_x was evaluated using X-ray photoelectron spectroscopy (XPS). As shown in Fig. 2b, the characteristic N, Li, Na, K, Rb, and Cs peaks confirm the successful anchoring of SAMs on the ITO/NiO_x substrate. In the Ni 2*p* spectra, the Ni^{3+} peak of bare ITO/NiO_x at 855.5 eV shifts to 855.8 eV after SAM deposition (Supplementary Fig. 47), indicating strong coordination between Ni atoms and the -P-O moieties of SAMs, which enhances anchoring stability and facilitates hole transfer[33]. From the integrated peak areas (Fig. 2c-e), the Ni^{3+}/Ni^{2+} ratio increases from 1.47 (NiO_x) to 2.34 (NiO_x/Me-4PACz) and 2.49 (NiO_x/Me+K), suggesting improved NiO_x conductivity, consistent with the O 1*s* spectra trend (Supplementary Fig. 48). Based on the P/Ni peak-area ratios, the surface coverage factors of ITO/NiO_x/Me-4PACz and ITO/NiO_x/Me+K are 2.8% and 4.7%, respectively (Fig. 2f). These results indicate that 2PACz-K reduces Me-4PACz self-aggregation via π–π interactions, resulting in denser molecular packing and enhanced interfacial coverage.

To elucidate the influence of SAMs on perovskite crystallization and interfacial coupling, the buried perovskite interface was exposed. XPS spectra of Ni 2*p* and O 1*s* reveal strengthened interfacial bonding, reduced trap density, and improved conductivity (Supplementary Fig. 49). The Pb 4*f* peaks shift toward lower binding energies, reflecting coordination between Pb^{2+} and the carbazole moieties of 2PACz-K (Fig. 2g, Supplementary Fig. 50). Morphological analyses show that the buried interface based on ITO/NiO_x/Me-4PACz contains cracks and voids (Fig. 2h, Supplementary Fig. 51), whereas that of ITO/NiO_x/Me+K exhibits a compact and smooth morphology. Correspondingly, the top perovskite films grown on Me+K display larger grains and fewer boundaries compared with those on Me-4PACz (Supplementary Fig. 52). Enhanced crystallinity and superior crystal quality in Me+K-based films are further confirmed by GIWAXS, XRD, and UV-vis measurements (Fig. 2i, Supplementary Fig. 53-54), demonstrating that the synergistic SAM engineering effectively improves buried interfacial quality and overall film formation. Additionally, considering the molecular arrangement patterns simulated by molecular dynamics, Me-4PACz suffers from aggregation and desorption, leading to the formation of nanovoids at the buried interface of perovskite (Fig. 2j-m, Supplementary Fig. 55). While 2PACz-K reduces the agglomeration of Me-4PACz, increases the surface coverage of NiO_x/ITO and delivers a more compact synergistic SAM layer.

Charge transfer and defect suppression

When functioning as hole-transporting materials, neutral SAMs receive holes from perovskite layers (i.e., donate electrons) through a single-electron transfer process[50,51], forming radical cations (Fig. 3a). The spin density describes the spatial distribution of unpaired electrons. Owing to the electron-rich nature of carbazole, it readily loses electrons to generate cationic radicals; therefore, the spin density is mainly localized on the carbazole rings for both Me-4PACz and 2PACz-K (Fig. 3b, Supplementary Fig. 56). In contrast, for 2PACz-K, part of the spin density extends to the phosphonate group, and this delocalization facilitates hole extraction and transport along the

molecular backbone. As shown in Supplementary Fig. 57, the nitrogen atom in Me-4PACz exhibits a higher spin population (0.293) than that in 2PACz-K (0.249). This localized spin density implies higher reactivity, potentially leading to C–N bond cleavage and compromising device stability[51].

According to Marcus theory and DFT calculations (Supplementary Fig. 58)[52], the dimer reorganization energy (ROE) of 2PACz-K (0.848 eV), is lower than that of Me-4PACz (0.931 eV). The reduced ROE indicates enhanced hole mobility and decreased energetic disorder in 2PACz-K[47], which helps suppress non-radiative recombination and minimize current leakage (Supplementary Fig. 59).

The interfacial contact and charge-transfer characteristics of mixed SAMs were further examined by atomic force microscopy (AFM) and Kelvin probe force microscopy (KPFM). The Me+M films show lower surface roughness than Me-4PACz (Fig. 3c, Supplementary Fig. 60), as the latter tends to aggregate and deteriorate surface coverage[22]. Notably, the Me+K film exhibits the lowest roughness, implying the best interfacial conformity. Additionally, the contact potential difference (CPD) of mixed SAMs shifts to more negative values compared with Me-4PACz (Supplementary Fig. 61). Among them, the Me+K film exhibits the lowest contact potential and the narrowest CPD distribution (Fig. 3d, Supplementary Fig. 62-63), reflecting the smallest interfacial barrier and most efficient hole extraction, thereby reducing nonradiative recombination in devices[53].

Ultraviolet photoelectron spectroscopy (UPS) measurements (Fig. 3e, Supplementary Fig. 64) reveal that the Me+K film has a deeper Fermi level (-5.08 eV) than Me-4PACz (-5.01 eV), in the same trend with the KPFM potential mapping. The enlarged work function of Me+K suggests stronger p-type characteristics, promoting hole extraction from the perovskite layer. Moreover, the smaller energy offset between the HOMO level of SAMs and the valence band maximum (VBM) of the perovskite for Me+K (0.41 eV) compared with Me-4PACz (0.57 eV) facilitates more efficient hole transport and contributes to enhanced device performance.

The optoelectronic properties of the perovskite films were evaluated by steady-state photoluminescence (PL) spectroscopy and PL mapping. As shown in Supplementary Fig. 65, the

perovskite films deposited on mixed SAMs exhibit stronger PL intensity, with the Me+K-based perovskite showing the highest emission. Confocal PL mapping further confirms that the perovskite films on Me+K exhibit higher PL intensity, narrower emission wavelength distribution, and a smaller full width at half maximum (FWHM) compared with those on Me-4PACz (Fig. 3f), indicative of suppressed non-radiative recombination. This defect-suppression effect arises because the highly delocalized π-electrons in 2PACz-K can effectively interact with undercoordinated Pb^{2+} ions at the bottom perovskite interface. Moreover, the reduced aggregation of Me-4PACz and improved interfacial uniformity afforded by 2PACz-K collectively lead to lower defect density and enhanced interfacial quality in the perovskite layer.

Photovoltaic performance of PSCs and modules

We investigated the device performance of small-area PSCs and perovskite solar modules (PSMs) with the configuration of ITO/NiO_x/SAM/perovskite/PDADI/C_{60}/BCP/Ag. Sequentially deposited Me-4PACz and 2PACz-K were employed in PSCs, leading to higher PCE and a lower hysteresis index (HI) compared to Me-4PACz alone (Supplementary Fig. 66). The champion device based on Me-4PACz achieved a PCE of 23.41%, whereas the mixed Me-4PACz+2PACz-K systems reached PCEs between 25% and 26%, depending on the blending ratio (Supplementary Fig. 67). The optimal composition was identified as a 4:1 molar ratio of Me-4PACz to 2PACz-K with a total concentration of 1 mmol/L. The performance enhancement of the mixed SAMs over Me-4PACz (Fig. 4a-b, Supplementary Fig. 68, Supplementary Table 2) is consistent with improved interfacial quality and more efficient charge transfer.

Furthermore, we employed presynthesized $FAPbI_3$, $MAPbI_3$ and $CsPbI_3$ single crystals as solutes to fabricate devices for reduced defects and high purity (Supplementary Fig. 69). The champion Me+K device delivered a PCE of 26.88%, with a V_{OC} of 1.177 V, a J_{SC} of 26.39 mA cm^{-2}, and an enhanced FF of 86.57%, exhibiting negligible hysteresis (Fig. 4c, Supplementary Fig. 70). This represents one of the highest efficiencies reported for inverted PSCs using SAM-based hole-transport layers (Fig. 4d, Supplementary Fig. 71, Supplementary Table 3). In comparison, the

best Me-4PACz device yielded a lower PCE of 24.90%, with a V_{OC} of 1.156 V, a J_{SC} of 26.21 mA cm^{-2}, an FF of 82.19% and an HI of 3.7%. The mixed-SAM strategy thus resulted in an average improvement of 20 mV in V_{OC} and 4% in FF (Fig. 4e, Supplementary Table 4), attributable to optimized interfacial contact, more efficient hole transport, and suppressed electronic defects as discussed earlier. The external quantum efficiency (EQE)-integrated J_{SC} values were 25.21 and 25.54 mA cm^{-2} for Me-4PACz and Me+K devices, respectively (Supplementary Fig. 72), in good agreement with the J_{SC} obtained from J–V scans.

To assess the scalability of the mixed-SAM strategy, mini-modules with dimensions of 6.5 cm × 7.0 cm were fabricated. As shown in Fig. 4f, the module comprising eight series-connected subcells with an aperture area of 29.7 cm^2 achieved a champion PCE of 23.32%, with a V_{OC} of 9.483 V, a J_{SC} of 2.945 mA cm^{-2}, and an FF of 83.49% under reverse scan. The backside of the module exhibited a smooth, mirror-like surface (Fig. 4g), confirming excellent film uniformity and controlled crystallization. The incorporation of 2PACz-K effectively suppresses SAM aggregation and ensures complete coverage with improved hole-transport characteristics, as reported previously[23,29,54]. Consequently, this approach yields outstanding efficiency across modules of varying area (Fig. 4h, Supplementary Fig. 73, Supplementary Table 5).

Stability of SAMs and devices

The stability of SAM materials and devices plays a crucial role in determining the long-term performance and cost of PSCs. We examined the stability of Me-4PACz and 2PACz-K under UV irradiation, thermal stress, and external electric fields using both theoretical calculations and experimental analyses. The UV stability was assessed by ^{1}H NMR measurements before and after 24 hours of UV exposure. Me-4PACz exhibited pronounced changes in the aromatic region between 7 and 8 ppm (Fig. 5a), suggesting cleavage of the carbazole ring and thus its photoinstability[13]. In contrast, 2PACz-K showed negligible chemical-shift variation after UV soaking (Fig. 5b).

To further elucidate the intrinsic photostability, a series of DFT calculations were performed.

For Me-4PACz and 2PACz, the calculated HOMO and LUMO are primarily localized on the electron-rich carbazole moiety (Supplementary Fig. 74), where the high-energy excited state facilitates photochemical reactions[55]. In contrast, the HOMO and LUMO of 2PACz-K are significantly delocalized and spatially separated, which enhances photostability through charge delocalization. In addition, excitation energies and oscillator strengths of the excited states for both SAMs were computed using the time-dependent DFT (TD-DFT) method[56]. The oscillator strengths of 2PACz-K are approximately one order of magnitude lower than those of Me-4PACz and 2PACz (Supplementary Tables 6-7, Supplementary Fig. 75), indicating that 2PACz-K is less likely to absorb photons of the corresponding frequencies and undergo excited-state transitions. The reduced electron–hole overlap further supports the superior stability of 2PACz-K in its excited states (Supplementary Fig. 76). The calculated photo-decomposition energy diagrams and proposed mechanism also confirm the higher UV resistance of 2PACz-K as well as the mixture of Me-4PACz+2PACz-K (Supplementary Fig. 77-78), which concurrently mitigates perovskite degradation[51,57].

Moreover, thermogravimetric (TG) analyses reveal that 2PACz-K exhibits higher thermal stability than 2PACz and Me-4PACz (Supplementary Fig. 79). AIMD simulations were performed by ORCA to theoretically confirm the thermal stability. Isomerization and dissociation are not observed at 373, 1000 and 2000 K for both Me-4PACz and 2PACz-K (Supplementary Fig. 80), while larger geometry fluctuation is observed with higher simulation temperature. Comparatively, Me-4PACz suffers from more prominent structural distortion and cleavage than 2PACz-K under 5000 K thermostat (Fig. 5c-d, Supplementary Fig. 81-83, Supplementary Movies 5-6).

The poor reverse-bias stability of PSCs has been a bottleneck for real-world applications, as partial shading of a module can induce irreversible damage[58,59]. To address this, we theoretically evaluated the effect of external electric fields (EEF) on Me-4PACz and 2PACz-K. According to intrinsic reaction coordinate (IRC) curves and downhill trajectories (Supplementary Fig. 84, Supplementary Movies 7-8), both molecules exhibit geometric deformation rather than bond cleavage under the applied EEF[60]. Charge accumulation and depletion occur due to the dense

electron cloud within the SAM molecules, as shown by the electron density difference maps (Supplementary Fig. 85-87). Furthermore, 2PACz-K exhibits larger dipole moments than Me-4PACz under both positive and negative electric fields (Supplementary Fig. 88), facilitating hole extraction as discussed earlier. Under EEF, the ALIE minima of 2PACz-K are smaller than those of Me-4PACz (Supplementary Fig. 88-90), indicating that the electrons in 2PACz-K are more weakly bound within the carbazole fragment. These delocalized π-electrons thus promote hole transport under operational conditions. Overall, 2PACz-K exhibits superior UV, thermal, and electrical-field stability compared to Me-4PACz. Consequently, incorporating 2PACz-K into Me-4PACz yields improved overall device durability.

The changes in CPD of SAM films under various aging conditions were further examined by KPFM. Both Me-4PACz and Me+K films demonstrate favorable thermal stability; however, Me-4PACz shows more pronounced CPD variation after DMF washing and UV aging compared to Me+K (Fig. 5e, Supplementary Fig. 91-92). This can be attributed to aggregation and weak anchoring of Me-4PACz on NiO_x, making it more susceptible to solvent or UV-induced disruption and hence device degradation[22]. In contrast, mixed SAMs form stronger anchoring on NiO_x and more robust interfacial contact, ensuring stability under harsh conditions.

The stability of the corresponding perovskite films and devices was also evaluated. As shown in XRD patterns (Fig. 5f-g, Supplementary Fig. 93), perovskite films employing Me+K show less degradation under thermal or humid environments. Steady-state PL evolution and PL mapping of illumination-aged films (Supplementary Fig. 94-95) reveal that samples based on Me-4PACz suffer from reduced PL intensity, broader emission spectra, and wider FWHM after aging—indicative of ion migration, phase segregation, and film degradation[6,61]. These effects are substantially mitigated in Me+K-based films owing to improved interfacial quality and suppressed defect formation.

According to the ISOS-L-1 stability protocol, the unencapsulated Me+K-based device retained 80% of the initial PCE after 1050 h at maximum power point (MPP) tracking under 1-sun equivalent illumination at 25 °C in nitrogen (Fig. 5h). Following the ISOS-D-1 protocol[29,62], the

Me+K-based device retained 95% of the initial PCE after 1020 h, corresponding to a T_{80} lifetime of 3916 h (Supplementary Fig. 96). Under the ISOS-D-2 test, the unencapsulated Me+K device maintained 92% of its initial PCE for 520 h, extrapolated to a T_{80} of 1297 h—outperforming the Me-4PACz-based device (Fig. 5i). In summary, the mixed-SAM strategy establishes a robust perovskite bottom interface, enabling durable and stable photovoltaic operation.

Wide-bandgap PSCs and tandem devices

The universality of the above SAM synergy strategy was further examined across perovskites with diverse bandgaps and SAM chemistries. MA-free 1.65 eV devices based on Me-4PACz+2PACz-K achieved a champion PCE of 23.76% with a FF of 84.48% under reverse scan (Supplementary Fig. 97). Similarly, 1.67 eV devices employing Me-4PACz+2PACz-K exhibited a PCE of 22.80% and an FF of 85.38%, corresponding to 93.9% of the Shockley–Queisser (S–Q) limit (Supplementary Fig. 98, Supplementary Table 8). These exceptionally high FF values for 1.55, 1.65, and 1.67 eV devices stem from the improved interfacial quality, enhanced hole transport, and suppressed interfacial defects discussed above.

Beyond these specific systems, the SAM synergy strategy was also extended to other SAM combinations. IGMH maps (Fig 6a, Supplementary Fig. 99) reveal clear π–π interactions between 4PADCB and 2PACz-K, which promote ordered molecular packing and denser SAM formation. The 1.78 eV device incorporating 4PADCB+2PACz-K (target) achieved a champion PCE of 20.27% (certified 20.75%) in Fig 6b and Supplementary Fig. 100-101, surpassing the 19.46% obtained for the 4PADCB-only control. Wide-bandgap (WBG) perovskite films grown on mixed SAMs exhibited enhanced crystallinity and phase purity (Supplementary Fig. 102), thereby contributing to the improved device performance. Similarly, the mixed SAMs of 2F+2PACz-K were applied to a narrow-bandgap (NBG) 1.25 eV Sn–Pb PSC[63], yielding a champion PCE of 22.75% (Supplementary Fig. 103). Collectively, these results demonstrate that the SAM synergy strategy is compatible with a variety of SAM molecular systems, perovskite compositions, and bandgaps, enabling superior device efficiencies and fill factors (Fig 6c, Supplementary Fig. 104-105).

WBG perovskites often suffer from phase heterogeneity, severe bulk and interfacial non-radiative recombination, and halide ion migration, all of which deteriorate device performance and stability[64]. WBG mixed-halide perovskites with high Br/I ratios (>20%) tend to undergo photo-induced phase segregation[65], leading to the formation of I-rich reduced-bandgap and Br-rich increased-bandgap domains. The light stability of WBG films was thus evaluated through steady-state PL evolution. The 1.67 eV perovskite based on Me-4PACz+2PACz-K exhibited negligible phase segregation under both 1-sun equivalent illumination and 85 °C heating (Supplementary Fig. 106). In contrast, control 1.78 eV films displayed pronounced PL quenching and the emergence of I-rich peaks (Fig 6d-g, Supplementary Fig. 106), indicating severe light-induced phase segregation. The target films, however, showed only a slight redshift and limited PL quenching. This suppressed phase segregation and improved photostability are attributed to the dense interfacial contact and reduced initial defect density provided by the robust 2PACz-K SAM (Supplementary Fig. 107).

To further confirm the universality of the SAM synergy strategy, 2-terminal (2T) all-perovskite tandem solar cells (TSCs) were fabricated, employing 4PADCB+2PACz-K for the 1.78 eV WBG top cell and 2F+2PACz-K for the 1.25 eV NBG bottom cell. As shown in Fig. 6h, the best-performing tandem achieved an impressive PCE of 29.05% (28.50%), with a V_{OC} of 2.148 V (2.148 V), a J_{SC} of 16.52 mA cm^{-2} (16.58 mA cm^{-2}), and an FF of 81.87% (80.00%) under reverse (forward) scans. The EQE-integrated J_{SC} values for the WBG and NBG subcells were 16.04 and 15.71 mA cm^{-2}, respectively (Fig. 6i). These PCE and V_{OC} values rank among the highest for all-perovskite TSCs to date (Fig. 6j, Supplementary Table 9), underscoring the superiority of the SAM synergy approach. Moreover, under the ISOS-L-1 stability protocol, the target tandem device retained 90% of its initial efficiency after 720 hours of continuous operation under 1-sun equivalent illumination at MPP in nitrogen (Supplementary Fig. 108).

In summary, we have developed a class of alkali metal ion 2PACz-M salt SAMs through head-group functionalization of 2PACz, which effectively enhances π-electron delocalization and introduces ionic characteristics into the non-acidic neutralized phosphonate group. Furthermore,

the synergistic combination of Me-4PACz and 2PACz-K enables optimized interfacial contact, efficient hole extraction, and multifaceted stability. The champion 1.55 eV PSC achieves a remarkable PCE of 26.88% with an FF of 86.57%, while the corresponding module with an aperture area of 29.7 cm^2 delivers an impressive PCE of 23.32%. More importantly, the universality of the SAM synergy strategy ensures superior performance across PSCs with different bandgaps, and the two-terminal tandem solar cells exhibit a state-of-the-art PCE of 29.05%. This work provides distinctive insights into the molecular design of ionic SAMs, offering a versatile pathway toward highly efficient and intrinsically stable perovskite photovoltaics.

Methods

Materials

For the materials used for perovskite solar cells fabrication, all materials were obtained from commercial suppliers and used without any purification. Formamidinium iodide (FAI, 99.99%), formamidinium bromide (FABr, 99.99%), methylammonium chloride (MACl, 99.99%) and methylammonium iodide (MAI, 99.99%) were purchased from Greatcell Solar. Lead (II) iodide (PbI_2, 99.9%), 4PADCB, 2PACz and Me-4PACz were purchased from Tokyo Chemical Industry Co., Ltd. (TCI). Cesium iodide (CsI, 99.9%), lead bromide ($PbBr_2$, 99.9%), 1,3-diaminopropane dihydroiodide (PDADI), C_{60} and BCP were purchased Xi'an Polymer Light Technology Corp (Xi'an Yuri Solar Co., Ltd). Pre-patterned ITO substrates were purchased from Advanced Election Technology Co., Ltd. Nickel oxide (NiO_x) nanoparticle powder and $CsPbI_3$ were purchased from Zhoushan Huazhou Chemical Co., Ltd. Tin (II) iodide (SnI_2, 99.999%), tin (II) flourine (SnF_2, 99%), ammonium thiocyanate (NH_4SCN), isopropanol (IPA, 99.9%), chlorobenzene (CB, 99.9%), *N*,*N*-dimethyl formamide (DMF, 99.8%), pure ethanol (EtOH, 99.8%) and dimethyl sulfoxide (DMSO, 99.8%) were purchased from Sigma-Aldrich. Ethyl acetate (EA, 99%) was purchased from Macklin. 1-aza-18-crown-6-ether (A18C6, 98%) and γ-butyrolactone (GBL) were purchased from Aladdin.

Synthesis of $MAPbI_3$, $FAPbI_3$, and $MAPbBr_3$ single crystals

$MAPbI_3$, $FAPbI_3$ and $MAPbBr_3$ were grown by inverse temperature crystallization (ITC) method. After collecting the crystals, the mother liquor can be reserved for recycling use.

For $MAPbI_3$, 1.271 g of MAI and 3.688 g of PbI_2 were dissolved in 7 mL of GBL and stirred overnight at 60 ℃. The hot solution was rapidly filtered by 0.45 μm nylon filters and heated on a hot plate (from 60 ℃ to 150 °C, rise 1 centigrade per minute). The shiny black dodecahedral-shaped single crystals ($MAPbI_3$) were grown in GBL solution, followed by vacuum drying (the yield of $MAPbI_3$ was ~30%).

For $FAPbI_3$, 2.236 g of FAI, 5.993 g of PbI_2 were dissolved in 10 mL of GBL and stirred overnight at room temperature. After complete dissolution, the yellow solution was filtered and heated on a hot plate (from 25 ℃ to 160 °C, rise 1 centigrade per minute). The shiny black single crystals (α-$FAPbI_3$) were grown in GBL solution, followed by vacuum drying (the yield of $FAPbI_3$ was ~30%).

For $MAPbBr_3$, 1.119 g of MABr, 3.670 g of $PbBr_2$ were dissolved in 10 mL of DMF and stirred overnight at room temperature. After complete dissolution, the colorless solution was filtered and heated on a hot plate (from 25 ℃ to 120 °C, rise 1 centigrade per minute). The bright orange nanocubes ($MAPbBr_3$) were grown in DMF solution, followed by vacuum drying (the yield of $MAPbBr_3$ was ~50%).

Precursor Preparation

For typical bandgap (1.55 eV) perovskite, a 1.6 mol/L perovskite precursor solution with a composition of $Cs_{0.05}(FA_{0.95}MA_{0.05})_{0.95}PbI_3$ was prepared by dissolving stoichiometric amounts of FAI, MAI, PbI_2 and CsI and 10 % MACl in a mixed anhydrous solvent of DMF and DMSO (volume ratio 4:1). For high-efficiency devices, presynthesized $CsPbI_3$, $FAPbI_3$ and $MAPbI_3$ replace CsI, FAI, MAI and PbI_2 in precursor solution.

For typical bandgap (1.65 eV) perovskite, a 1.5 mol/L perovskite precursor solution with a composition of $Cs_{0.17}FA_{0.83}Pb(I_{0.8}Br_{0.2})_3$ was prepared by dissolving stoichiometric amounts of CsI, FAI, PbI_2 and $PbBr_2$ in a mixed anhydrous solvent of DMF and DMSO (volume ratio 4:1).

For wide bandgap (1.67 eV) perovskite, a 1.5 mol/L perovskite precursor solution with a composition of $Cs_{0.05}FA_{0.73}MA_{0.22}Pb(I_{0.77}Br_{0.23})_3$ was prepared by dissolving stoichiometric amounts of $PbBr_2$, CsI, PbI_2, $MAPbBr_3$ and $FAPbI_3$ in a mixed anhydrous solvent of DMF and DMSO (volume ratio 4:1).

For wide bandgap (1.78 eV) perovskite, a 1.2 mol/L perovskite precursor solution with a composition of $Cs_{0.2}FA_{0.8}Pb(I_{0.6}Br_{0.4})_3$ was prepared by dissolving stoichiometric amounts of FAI, CsI, FABr, PbI_2 and $PbBr_2$ in a mixed solvent of DMF and DMSO (volume ratio 3:1).

For narrow bandgap (1.25 eV) perovskite[66], a 1.8 mol/L perovskite precursor solution with a composition of $Cs_{0.1}FA_{0.6}MA_{0.3}Pb_{0.5}Sn_{0.5}I_3$ was prepared by dissolving PbI_2 (414.9 mg), SnI_2 (335.2 mg), FAI (185.7 mg), MAI (85.8 mg), CsI (46.7 mg), SnF_2 (14.1 mg), and NH_4SCN (2.7 mg) in 1 ml mixed solvent of DMF and DMSO with a volume ratio of 3:1.

For all the perovskite precursor solutions, A18C6 was used as an additive with the concentration of 0.4 mmol/L. A18C6 contributes to perovskite precursor stabilization, defect passivation and enhanced moisture stability[6,67]. All of the solutions were filtered by 0.22 μm filters before use.

Device fabrication

For single-junction PSCs, pre-patterned ITO glass substrates were cleaned with deionized water, anhydrous alcohol and acetone using an ultrasonic cleaner. The ITO substrates were dried and treated with oxygen plasma for 5 min prior to use. The NiO_x layer was fabricated by spin-coating 10 mg/mL NiO_x solution (dispersed in deionized water) onto ITO substrates at 3000 rpm for 30 s, and annealed at 140 °C for 10 min in ambient air. Then the substrates were transferred into N_2-filled glove box. The solutions of SAM materials (Me-4PACz, 2PACz, 4PADCB, 2F, 2PACz-M or mixed SAMs) were dissolved in mix solvent of ethanol and DMF (volume ratio 10:1) with a total concentration of 1 mmol/L. The solution was spin-coated onto the ITO substrates at 3000 rpm for 30 s, followed by annealing at 100 °C for 10 min. Subsequently, 50 μL of perovskite precursor solutions were spin-coated at 5000 rpm for 40 s. During the spin-coating process, ~200

μL EA was rapidly dropped onto the substrates at 30 s, followed by annealing at 100 ℃ for 10-30 min. The PDADI solution (0.5 mg/mL in IPA) was then spin-coated onto the perovskite layer at 5000 rpm for 30 s and annealed at 100 °C for 3 min. Finally, 25 nm layer of C_{60}, 7 nm layer of BCP, and 120 nm Ag were thermally evaporated in a high-vacuum chamber through a metal shadow mask with an aperture area of 0.04 cm^2 .

For target tandem solar cells, the structure is ITO / NiO_x / 4PADCB+2PACz-K / 1.78 eV PVK / PDADI / C_{60} / ALD-SnO_2 / IZO / 2F+2PACz-K / 1.25 eV PVK / PDADI / C_{60} / BCP / Ag. The preparation of the bottom subcell was the same as the fabrication of 1.78 eV wide bandgap PSCs before the thermal evaporation of BCP. Then the substrates were deposited 30 nm SnO_2 by the atomic layer deposition (ALD), and transferred into the magnetron sputtering system to sputter 100-nm IZO. Next, 2F+2PACz-K solution was spin-coated onto the substrates at 3000 rpm for 30 s and then annealed at 100 °C for 10 min in nitrogen. The perovskite precursor was spin-coated with the two-step process of 1000 rpm for 10 s and 4000 rpm for 50 s. During the spin-coating process, ~500 μL CB was dropped onto the substrates at 30 s, followed by annealing at 100 ℃ for 10 min. The PDADI solution (0.5 mg/mL in IPA) was then spin-coated onto the perovskite layer at 4000 rpm for 30 s and annealed at 100 °C for 5 min. Finally, 20 nm layer of C_{60}, 6 nm layer of BCP, and 120 nm Ag were thermally evaporated in a high-vacuum chamber.

For mini-module fabrication, the perovskite solar modules consisting of 8 sub-cells connected in series were fabricated on ITO glass substrates. All three scribes (P1, P2, P3) were made with the near-infrared 1064 nm 20 W laser (Trotec). 6.5 cm × 7 cm ITO substrates were patterned by a laser with a scribing width of 40 μm (speed: 300 $mm \cdot s^{-1}$; frequency: 65 kHz; pulse duration: 120 ns; power: 60%). The ITO substrates were cleaned and treated with plasma. The following fabrication process of NiO_x, SAM, perovskite, C_{60} and BCP was the same as that of small area devices. Then the substrates were laser scribed over a width of 400 μm (multiple parallel scribes with 50 μm spacing, speed: 1000 $mm \cdot s^{-1}$; pulse duration: 120 ns; frequency: 65 kHz, power: 15%). Finally, 80 nm Ag electrode was deposited by thermal evaporation and scribed by a laser with a width of 50 μm (speed: 1000 $mm \cdot s^{-1}$; pulse duration: 120 ns; frequency: 65 kHz; power: 15%).

The designed geometric fill factor of the modules was ~92% with an aperture area (AP) of 29.7 cm^2.

Characterization and measurements

For SAM synthesis, ^1H NMR spectra were recorded at 400 MHz on a Bruker Avance III spectrometer with a 5 mm double resonance broad band BBO z-gradient room temperature probe, ^{13}C NMR spectra were collected using the same instrument at 101 MHz. The chemical shifts, expressed in ppm, were relative to tetramethylsilane (TMS). All NMR experiments were performed at 25 °C. Mass spectrometry (MS) were recorded on Waters SQ Detector 2 Spectrometer using the electrospray ionization (ESI) technique.

Generally, absorption spectra were measured using a UV/Vis-NIR spectrophotometer, Lambda 35 (Perkin-Elmer). Photoelectron spectroscopy in air (PESA) was measured by Riken Keiki AC-2S. X-ray photoelectron spectroscopy (XPS) was performed by Thermo Scientific K-Alpha (Al Kα source), and all spectra were calibrated to the C 1s peak at 284.8 eV. Ultraviolet photo-electron spectroscopy (UPS) was performed by Thermo Fisher Scientific ESCALAB XI+. X-ray diffraction (XRD) patterns were measured by using a Rigaku Smartlab 9KW X-ray diffractometer. Scanning electron microscopy (SEM) images were obtained by using FEI Apreo S LoVac. Atomic force microscope (AFM) and Kelvin probe force microscopy (KPFM) were conducted by Bruker Dimension Icon instrument. Grazing incident wide angle X-ray scattering (GIWAXS) measurements were carried out on beamline BL14B1 at the Shanghai Synchrotron Radiation Facility (SSRF). Inductively coupled plasma mass spectrometry (ICP-MS) was measured by Agilent 7800 (MS). Thermogravimetry (TG) was measured by HITACHI STA200. Steady-state PL spectra were tested by using Edinburgh FLS1000. PL mapping was obtained by Confocal Microscopy (SPCM-1000) supported by Enli Technology Co., Ltd. The *J–V* characteristics of photovoltaic devices were measured with a solar simulator (Enli Technology) and Keithley 2400 source meter under AM 1.5 G standard irradiation (1000 W/m^2). Intensity of the solar simulator was calibrated using a certified monocrystalline silicon solar cell (KG5). The

active area are 0.04 cm^2 for single-junction devices and 0.09 cm^2 for tandem devices, defined by metal masks. Both reverse scans and forward scans were conducted. External quantum efficiency (EQE) was recorded on a solar cell quantum efficiency measurement system (QE-R) supported by Enli Technology. The EQE spectra of single-junction PSCs were performed from 300 to 900 nm, and a calibrated Si diode with a known spectral response was used as a reference. The EQE spectra were performed from 300 to 1100 nm for TSCs. For the EQE measurements of TSCs, a white light was used as the external light source with the 550 and 850 nm filters for NBG and WBG subcells, respectively. Specifically, the wave range of 550–1100 nm and 300–850 nm was utilized for NBG and WBG subcells, respectively. The MPP tracking was performed with a multicolor light-emitting diode solar simulator (Guangzhou Crysco Equipment Co. Ltd.) with 100 mW cm^{-2} irradiation.

Computational Details

All density functional theory (DFT) calculations were performed using Gaussian or ORCA software[68]. Geometries optimization and energy analyses were performed based on the B3LYP functional with Grimme's D3 (BJ) dispersion correction in conjunction with def2-TZVP basis set[69]. The dipole moment was calculated via ωB97M-V functional with def2-TZVPD basis set. The binding energy was calculated via ωB97M-V functional with def2-QZVP basis set. The wave function analyses were finished via the Multiwfn 3.8(dev) code[34,35] and Visual Molecular Dynamics (VMD) visualization program. The *ab-initio* molecular dynamics (AIMD) were simulated by ORCA with B97-3c method under Berendsen thermostat. Multiwfn was used to help generate the input files for ORCA.

First-principles calculations based on DFT were conducted using the CP2K software[70]. Multiwfn was used to help generate the input files for CP2K. The Perdew–Burke–Ernzerhof (PBE) exchange-correlation functional with D3 (BJ) dispersion correction was employed, utilizing DZVP-MOLOPT-SR-GTH basis set paired with corresponding Goedecker–Teter–Hutter (GTH) pseudopotentials[71]. The plane wave cut-off was set to 500 Ry for the auxiliary basis set, and the Brillouin zone was sampled at the Γ point. Periodic boundary conditions were used in xy-direction,

and an auxiliary vacuum region of 20 Å along the z-direction was added. The energy convergence criterion for self-consistent field calculations was set to 10^{-5} eV, and the maximum force convergence criterion was set to 0.05 eV/Å. The ITO surface slab model was built based on the 21 Å × 21 Å × 7 Å In_2O_3 supercell containing 4 atomic layers. The cubic-phased $FAPbI_3$ (001) PbI_2-terminated surface slab model was built based on the 18 Å × 18 Å × 19 Å supercell containing 7 atomic layers. The wave function analyses were finished via the Multiwfn 3.8(dev) code.

For SAMs in solution, classical molecular dynamics (MD) simulations were performed with GROMACS[46] using GAFF force field within a cubic box measuring 10 × 10 × 10 nm^3. Periodic boundary conditions were applied to all directions. The restrained electrostatic potential—RESP2(0.5) charges were used as the atomic charges[72], computed by ORCA and Multiwfn. The forcefield parameters and topology files were created by Sobtop (http://sobereva.com/soft/Sobtop/) via modified Seminario (mSeminario) method based on calculated Hessian-matrix under B3LYP-D3(BJ)/def2-TZVP level[47]. Primarily, the SAMs and solvent molecules were randomly located in the whole box, built by Packmol. Then the system underwent initial energy minimization via the conjugated gradient (CG) method[73]. Subsequently, the system was simulated for 2 ns (i.e., 2000 ps) at 298.15 K under NPT ensemble with a time step of 2 fs under the Velocity-rescale thermostat and Berendsen barostat.

For SAMs on NiO/ITO substrates, classical molecular dynamics simulations were performed with GROMACS. GAFF force field was used for SAMs and UFF force field was used for NiO and ITO. Periodic boundary conditions were applied to the xy-direction, whereas the bottom NiO/ITO substrates were fixed. Two repulsive walls were set in z-direction (z=0 and z=max) in order to constrain the motion range of SAMs. The adsorption models include a 85 Å × 85 Å × 7 Å NiO supercell and a 95 Å × 95 Å × 5 Å ITO supercell. The REPEAT charges were used as the atomic charges for NiO/ITO, computed by CP2K. The restrained electrostatic potential (RESP) charges in vacuum were used as the atomic charges for SAMs, computed by ORCA and Multiwfn. The system was simulated for 2 ns at 298.15 K under canonical ensemble (NVT) ensemble with a time

step of 1 fs under the Velocity-rescale thermostat. The adsorption analyses for SAMs employed our in-house code with VMD program.

Data Availability

The data generated in this study are provided in the Supplementary Information/Source Data file.

References

[1] Li, W. et al. Suppressing halide segregation of wide bandgap perovskite by interface molecular coordination for high-performance all-perovskite tandem solar cells. *Angew. Chem., Int. Ed.* **64**, e202511743 (2025).

[2] Jiang, Q. & Zhu, K. Rapid advances enabling high-performance inverted perovskite solar cells. *Nat. Rev. Mater*. **9**, 399-419 (2024).

[3] Best research-cell efficiency chart. https://www.nrel.gov/pv/cell-efficiency (2026)

[4] Chen, P. et al. The promise and challenges of inverted perovskite solar cells. *Chem. Rev.* **124**, 10623-10700 (2024).

[5] Gao, D. et al. High-efficiency perovskite solar cells enabled by suppressing intermolecular aggregation in hole-selective contacts. *Nat. Photonics* **19**, 1070-1077 (2025).

[6] Zhang, Z. et al. Coordination engineering with crown ethers for perovskite precursor stabilization and defect passivation. *Energy Environ. Sci.* **17**, 7182-7192 (2024).

[7] Li, Z. et al. Synthesis of a lattice-resolved laminate-structured perovskite heterointerface. *Nat. Synth.* **4**, 1078-1087 (2025).

[8] You, S. et al. C_{60}-based ionic salt electron shuttle for high-performance inverted perovskite solar modules. *Science* **388**, 964-968 (2025).

[9] Yang, Y. et al. Design and applications of hole-selective self-assembled monolayers for perovskite photovoltaics. *Chem. Eng. J.* **504**, 158870 (2025).

[10] Li, C. et al. Achieving 32% efficiency in perovskite/silicon tandem solar cells with bidentate-anchored superwetting self-assembled molecular layers. *Angew. Chem., Int. Ed.* **64**, e202502730 (2025).

[11] Tan, Q. et al. Inverted perovskite solar cells using dimethylacridine-based dopants. *Nature* **620**, 545-551 (2023).

[12] Zhao, K. et al. peri-Fused polyaromatic molecular contacts for perovskite solar cells. *Nature* **632**, 301-306 (2024).

[13] Liu, T. et al. Efficient perovskite solar modules enabled by a UV-stable and high-conductivity hole transport material. *Sci. Adv.* **11**, eadu3493 (2025).

[14] Wu, H. et al. Tailored lattice-matched carbazole self-assembled molecule for efficient and stable perovskite solar cells. *J. Am. Chem. Soc.* **147**, 8004-8011 (2025).

[15] Wu, W. et al. Stable and uniform self-assembled organic diradical molecules for perovskite photovoltaics. *Science* **389**, 195-199 (2025).

[16] Zheng, X. et al. Co-deposition of hole-selective contact and absorber for improving the processability of perovskite solar cells. *Nat. Energy* **8**, 462-472 (2023).

[17] Zhang, H. et al. Formamidinium lead iodide-based inverted perovskite solar cells with efficiency over 25 % enabled by an amphiphilic molecular hole-transporter. *Angew. Chem., Int. Ed.* **63**, e202401260 (2024).

[18] He, R. et al. Improving interface quality for 1-cm^2 all-perovskite tandem solar cells. *Nature* **618**, 80-86 (2023).

[19] Jiang, W. et al. π-Expanded carbazoles as hole-selective self-assembled monolayers for high-performance perovskite solar cells. *Angew. Chem., Int. Ed.* **61**, e202213560 (2022).

[20] Huang, C. et al. Electrostatically enhanced buried interface binding of self-assembled monolayers for efficient and stable inverted perovskite solar cells. *Adv. Mater.* **37**, e08740 (2025).

[21] Guo, H. et al. Neglected acidity pitfall: boric acid-anchoring hole-selective contact for perovskite solar cells. *Natl. Sci. Rev.* **10**, nwad057 (2023).

[22] Wang, J. et al. Less-acidic boric acid-functionalized self-assembled monolayer for mitigating NiO_x corrosion for efficient all-perovskite tandem solar cells. *Nat. Commun.* **16**, 4148 (2025).

[23] Zhang, S. et al. Minimizing buried interfacial defects for efficient inverted perovskite solar cells. *Science* **380**, 404-409 (2023).

[24] Yu, X., Sun, X., Zhu, Z. & Li, Z. Stabilization strategies of buried interface for efficient SAM-based inverted perovskite solar cells. *Angew. Chem., Int. Ed.* **64**, e202419608 (2025).

[25] Li, M., Liu, M., Qi, F., Lin, F. R. & Jen, A. K. Y. Self-assembled monolayers for interfacial engineering in solution-processed thin-film electronic devices: design, fabrication, and applications. *Chem. Rev.* **124**, 2138-2204 (2024).

[26] Sun, A. et al. High open-circuit voltage (1.197 V) in large-area (1 cm^2) inverted perovskite solar cell via interface planarization and highly polar self-assembled monolayer. *Adv. Energy Mater.* **14**, 2303941 (2024).

[27] Liu, S. et al. Buried interface molecular hybrid for inverted perovskite solar cells. *Nature* **632**, 536-542 (2024).

[28] Shi, C. et al. Modulating competitive adsorption of hybrid self-assembled molecules for efficient wide-bandgap perovskite solar cells and tandems. *Nat. Commun.* **16**, 3029 (2025).

[29] Zhang, Z. et al. Monodisperse regulation of self-assembled monolayer via dipole molecules for efficient perovskite solar cells. *Angew. Chem., Int. Ed.* **64**, e202512660 (2025).

[30] Li, C. et al. Enhancing efficiency of industrially-compatible monolithic perovskite/silicon tandem solar cells with dually-mixed self-assembled monolayers. *Adv. Funct. Mater.* **34**, 2407805 (2024).

[31] Chen, J. et al. Determining the bonding-degradation trade-off at heterointerfaces for increased efficiency and stability of perovskite solar cells. *Nat. Energy* **10**, 181-190 (2025).

[32] Lin, Z. et al. Suppressing the interface photodegradation towards efficient and stable all perovskite tandem solar cells. *Angew. Chem., Int. Ed.* **64**, e202424825 (2025).

[33] Cao, Q. et al. Co-self-assembled monolayers modified NiO_x for stable inverted perovskite solar cells. *Adv. Mater.* **36**, 202311970 (2024).

[34] Lu, T. & Chen, F. Multiwfn: A multifunctional wavefunction analyzer. *J. Comput. Chem.* **33**, 580-592 (2012).

[35] Lu, T. A comprehensive electron wavefunction analysis toolbox for chemists, Multiwfn. *J. Chem. Phys.* **161**, 082503 (2024).

[36] Lu, T. & Chen, F. Atomic dipole moment corrected Hirshfeld population method. *J. Theor. Comput. Chem.* **11**, 163-183 (2012).

[37] Liu, Z., Lu, T. & Chen, Q. Intermolecular interaction characteristics of the all-carboatomic ring, cyclo[18]carbon: Focusing on molecular adsorption and stacking. *Carbon* **171**, 514-523 (2021).

[38] Yuan, S. et al. Conjugated bisphosphonic acid self-assembled monolayers for efficient and stable inverted perovskite solar cells. *J. Am. Chem. Soc.* **147**, 24662-24671 (2025).

[39] Mou, H. et al. Transient dipole strategy boosts highly oriented self-assembled monolayers for organic solar cells approaching 21% efficiency. *J. Am. Chem. Soc.* **147**, 21241-21251 (2025).

[40] Politzer, P., Murray, J. S. & Bulat, F. A. Average local ionization energy: A review. *J. Mol. Model.* **16**, 1731-1742 (2010).

[41] Pino-Rios, R., Inostroza, D., Cardenas-Jiron, G. & Tiznado, W. Orbital-weighted dual descriptor for the study of local reactivity of systems with (quasi-) degenerate states. *J. Phys. Chem. A* **123**, 10556-10562 (2019).

[42] Wu, Y. et al. Exploring the aromaticity differences of isoelectronic species of cyclo[18]carbon (C_{18}), $B_6C_6N_6$, and B_9N_9-the role of carbon atoms as connecting bridges. *Inorg. Chem.* **62**, 19986-19996 (2023).

[43] Lu, T. Visualization analysis of covalent and noncovalent interactions in real space. *Angew. Chem., Int. Ed.* **64**, e202504895 (2025).

[44] Fuster, F. & Grabowski, S. J. Intramolecular hydrogen bonds: the QTAIM and ELF characteristics. *J. Phys. Chem. A* **115**, 10078-10086 (2011).

[45] Duan, W. et al. A spatial structure regulation strategy modulated the solubility and compactness of novel face-on oriented bisphosphonate-anchored SAMs for efficient inverted perovskite solar cells. *Energy Environ. Sci.* **18**, 7231-7244 (2025).

[46] Páll, S., Abraham, M. J., Kutzner, C., Hess, B. & Lindahl, E. in 2nd International Conference on Exascale Applications and Software (EASC). 3-27 (2015).

[47] Weigend, F. & Ahlrichs, R. Balanced basis sets of split valence, triple zeta valence and

quadruple zeta valence quality for H to Rn: Design and assessment of accuracy. *Phys. Chem. Chem. Phys.* **7**, 3297-3305 (2005).

[48] Pei, F. et al. Inhibiting defect passivation failure in perovskite for perovskite/Cu(In,Ga)Se_2 monolithic tandem solar cells with certified efficiency 27.35%. *Nat. Energy* **10**, 824-835 (2025).

[49] Wang, Y.-D. et al. Regulating wide-bandgap perovskite face-on stacking in hybrid-deposited perovskite/organic tandem solar cells. *Nat. Commun.* **16**, 6142 (2025).

[50] Ponseca, C. S., Jr., Chabera, P., Uhlig, J., Persson, P. & Sundstrom, V. Ultrafast electron dynamics in solar energy conversion. *Chem. Rev.* **117**, 10940-11024 (2017).

[51] Yan, B. et al. Chiral aza-helicene phosphonic acids for stabilizing efficient perovskite-silicon tandem solar cells. *Angew. Chem., Int. Ed.* **64**, e202509279 (2025).

[52] Fan, Y., Du, J., Zhao, W., Ma, X. & Yu, X. Molecular insights into Marcuss theory: An Ab initio quantum chemistry computational lab practice for charge transfer kinetics pedagogy. *J. Chem. Educ.* **101**, 3418-3427 (2024).

[53] Tong, X. et al. Large orientation angle buried substrate enables efficient flexible perovskite solar cells and modules. *Adv. Mater.* **36**, 2407032 (2024).

[54] Liu, X. et al. Perovskite solar modules with high efficiency exceeding 20%: From laboratory to industrial community. *Joule* **9**, 102056 (2025).

[55] Zhang, S. et al. Conjugated self-assembled monolayer as stable hole-selective contact for inverted perovskite solar cells. *ACS Mater. Lett.* **4**, 1976-1983 (2022).

[56] Liu, Z., Lu, T. & Chen, Q. An sp-hybridized all-carboatomic ring, cyclo[18]carbon: Electronic structure, electronic spectrum, and optical nonlinearity. *Carbon* **165**, 461-467 (2020).

[57] Zhang, S. et al. Self-assembled π-conjugated hole-selective molecules for UV-resistant high-efficiency perovskite solar cells. *Angew. Chem., Int. Ed.* **64**, e202508782 (2025).

[58] Li, N. et al. Barrier reinforcement for enhanced perovskite solar cell stability under reverse bias. *Nat. Energy* **9**, 1264-1274 (2024).

[59] Xu, Z. et al. Reverse-bias resilience of monolithic perovskite/silicon tandem solar cells. *Joule* **7**, 1992-2002 (2023).

[60] Lu, T. & Chen, Q. Ultrastrong regulation effect of the electric field on the all-carboatomic ring cyclo[18]carbon. *Chemphyschem* **22**, 386-395 (2021).

[61] Zhu, H. et al. Long-term operating stability in perovskite photovoltaics. *Nat. Rev. Mater.* **8**, 569-586 (2023).

[62] Khenkin, M. V. et al. Consensus statement for stability assessment and reporting for perovskite photovoltaics based on ISOS procedures. *Nat. Energy* **5**, 35-49 (2020).

[63] Zhu, J. et al. A donor-acceptor-type hole-selective contact reducing non-radiative recombination losses in both subcells towards efficient all-perovskite tandems. *Nat. Energy* **8**, 714-724 (2023).

[64] Guo, Y., Tan, H. & Xu, B. Deciphering halide ion migration and performance loss in wide-bandgap perovskite solar cells: connection, mechanism, and solutions. *Energy Environ. Sci.* **18**, 8744-8755(2025).

[65] Yang, G. et al. Towards efficient, scalable and stable perovskite silicon tandem solar cells. *Nat. Photonics* **19**, 913-924 (2025).

[66] Zhu, J. et al. Custom-tailored hole transport layer using oxalic acid for high-quality tin-lead perovskites and efficient all-perovskite tandems. *Sci. Adv.* **10**, eadl2063 (2024).

[67] Yang, Y. et al. Passivation of positively charged cationic defects in perovskite with nitrogen-donor crown ether enabling efficient perovskite solar cells. *Chem. Eng. J*. **451**, 138962 (2023).

[68] Neese, F. The SHARK integral generation and digestion system. *J. Comput. Chem.* **44**, 381-396 (2023).

[69] Grimme, S., Antony, J., Ehrlich, S. & Krieg, H. A consistent and accurate ab initio parametrization of density functional dispersion correction (DFT-D) for the 94 elements H-Pu. *J. Chem. Phys.* **132**, 154104 (2010).

[70] Kühne, T. D. et al. CP2K: an electronic structure and molecular dynamics software package-Quickstep: efficient and accurate electronic structure calculations. *J. Chem. Phys.* **152**, 194103 (2020).

[71] Goedecker, S., Teter, M. & Hutter, J. Separable dual-space Gaussian pseudopotentials. *Phys.*

Rev. B **54**, 1703 (1996).

[72] Bayly, C. I. et al. A well-behaved electrostatic potential based method using charge restraints for deriving atomic charges: the RESP model. *J. Phys. Chem.* **97**, 10269-10280 (1993).

[73] Sheppard, D., Terrell, R. & Henkelman, G. Optimization methods for finding minimum energy paths. *J. Chem. Phys.* **128**, 134106 (2008).

Acknowledgements

We acknowledge the characterization of the Beamline 14B1 in the Shanghai Synchrotron Radiation Facility (SSRF) for grazing incident wide angle X-ray scattering (GIWAXS). We thank Scientific Compass for XPS, UPS, ICP-MS and TG measurements (www.shiyanjia.com). We appreciate Dr. Tian Lu at Beijing Kein Research Center for Natural Sciences for the free programs, including Multiwfn for comprehensive and splendid wave function analyses along with concisely generating the input files for CP2K and ORCA (http://sobereva.com/multiwfn/), as well as Sobtop for conveniently generating forcefield parameters and GROMACS topology files (http://sobereva.com/soft/Sobtop/).

Funding Statement

This work was financially supported by Sinomine Resource (Tianjin) Advanced Materials Co., Ltd (2024GKF-0077). Funded by the European Union. Views and opinions expressed are however those of the author(s) only and do not necessarily reflect those of the European Union or the European Climate, Infrastructure and Environment Executive Agency. Neither the European Union nor the granting authority can be held responsible for them. HEPAFLEX project has received funding from HORIZON Research and Innovation Actions under Grant Agreement no. 101122345. This work received funding from project “Mission-driven Implementation of Science and Innovation Programmes” (No. 02-002-P-0001), funded by the Economic Revitalization and Resilience Enhancement Plan “New Generation Lithuania”. This work was financially supported

by the National Natural Science Foundation of China (52461160298), the Engineering Featured Team Fund of Sichuan University (2020SCUNG102).

Author Contributions Statement

Y.X.Y. D.K. and Y.L.X. contributed equally. Y.X.Y. designed the experiments, fabricated PSCs, and contributed to DFT calculations and molecular dynamics simulations. D.K. studied alternative synthesis of 2PACz. Y.L.X. fabricated the tandem devices. X.H.L., Q.Q.Z., Y.D.X., H.T., E.K., Z.Y.G., and X.F. participated in sample preparation and characterization. K.R. synthesized the metal SAMs. B.Z., J.X.X., C.X.X., S.P.P., V.G., D.W.Z., K.R. and Y.Z. were involved in discussion and project coordination. K.R. and Y.Z. conceived the idea and guided the work. Y.X.Y. and Y.Z. wrote the manuscript draft, and all the authors contributed to the revision.

Competing Interests Statement

All the authors declare no competing interests.

Figure Legends/Captions (for main text figures)

Fig. 1. Molecular characteristics of 2PACz-M. a Chemical structures of 2PACz and 2PACz-M (2PACz-Li, 2PACz-Na, 2PACz-K, 2PACz-Rb and 2PACz-Cs). **b** Dipole moment values of 2PACz and 2PACz-M. **c** Electrostatic potential (ESP) distribution of 2PACz and 2PACz-K. **d** Minimum and maximum of ESP of 2PACz and 2PACz-K. **e** Average local ionization energy (ALIE) maps on van der Waals surface of 2PACz and 2PACz-K. **f** The independent gradient model analyses based on Hirshfeld partition of molecular density (IGMH) maps of 2PACz-K and PbI_2 with isosurface of 0.001 a.u. **g** Isosurface map of charge density difference (CDD) before and after 2PACz-K interact with PbI_2 with isovalue of 0.0005 a.u. Blue and pink isosurfaces correspond to electron accumulation and depletion, respectively. The number of transferred electrons is labeled. **h** IGMH analyses of 2PACz and 2PACz-K on perovskite slab with isosurface of 0.001 a.u. **i-j** The DFT-optimized atomic structure and CDD of 2PACz and 2PACz-K binding on **i** perovskite and **j** ITO.

Blue and pink isosurfaces correspond to electron accumulation and depletion, respectively. **k** Color-filled plane maps of electron localization function (ELF) for phosphonate acid fragments in 2PACz and 2PACz-K. **l** *J–V* curves of the champion devices based on 2PACz and 2PACz-M. **m-n** The molecular arrangement patterns of **m** Me-4PACz and **n** 2PACz-K in water simulated by molecular dynamics. **o-p** The molecular arrangement patterns of **o** Me-4PACz and **p** mix SAMs in EtOH simulated by molecular dynamics.

Fig. 2. Interactions between SAMs and perovskite. a Chemical structure and IGMH map with isosurface of 0.0005 a.u. for Me-4PACz and 2PACz-K. **b** High-resolution XPS spectra of N 1*s*, Li 1*s*, Na 1*s*, K 2*p*, Rb 3*d* and Cs 3*d* core levels of Me-4PACz and mixed SAMs (Me+M). **c-d** High-resolution XPS spectra of Ni 2*p* core level for **c** ITO/NiO_x/Me-4PACz and **d** ITO/NiO_x/Me-4PACz+2PACz-K. **e** The peak area ratios of Ni^{3+} and Ni^{2+} for NiO_x and NiO_x/SAM. **f** High-resolution XPS spectra of P 2*p* core level for ITO/NiO_x/Me-4PACz and ITO/NiO_x/Me-4PACz+2PACz-K. **g** High-resolution XPS spectra of Pb 4*f* core level for the buried interface of perovskite. **h** SEM images of the buried interface morphology for the perovskite films based on Me-4PACz and Me-4PACz+2PACz-K. All scale bars are 1 μm. **i** GIWAXS two-dimensional maps of the top surface for the perovskite films on Me-4PACz and Me-4PACz+2PACz-K. **j-m** Top and side views of molecular arrangement patterns simulated by molecular dynamics, including **j** Me-4PACz on NiO, **k** Me-4PACz+2PACz-K on NiO, **l** Me-4PACz on ITO and **m** Me-4PACz+2PACz-K on ITO. Hydrogen atoms of Me-4PACz and 2PACz-K are hided for easy observation.

Fig. 3. Charge transfer and defect suppression. a Schematic diagram clarifying how neutral Me-4PACz and 2PACz-K molecules generate cationic radicals via single electron transfer. **b** Spin density isosurface maps of Me-4PACz and 2PACz-K with isovalue of 0.002 a.u. The blue and yellow isosurfaces correspond to alpha and beta electrons. **c-d c** AFM and **d** KPFM images of Me-4PACz and Me-4PACz+2PACz-K films on ITO/NiO_x. R_a and R_q refer to arithmetic mean roughness and root mean square roughness, respectively. All scale bars are 500 nm. **e** Energy level

diagrams of the SAMs and perovskite. **f** PL mapping of perovskite films, including PL intensity, wavelength and full width at half maximum (FWHM), respectively. All scale bars are 10 μm.

Fig. 4. Photovoltaic performance of PSCs and modules. a The statistical distribution of PCE for the devices based on mixed SAMs. **b** *J–V* curves of the champion devices based on mixed SAMs under reverse scan. **c** *J–V* characteristics of the champion devices fabricated with presynthesized $FAPbI_3$, $MAPbI_3$ and $CsPbI_3$ under reverse scan. **d** PCE and V_{OC} × FF records of single-junction inverted PSCs based on SAMs. This work is marked by the red star. **e** The statistical distribution of PCE, V_{OC}, FF and J_{SC} of devices based on Me-4PACz and Me-4PACz+2PACz-K. **f** *J–V* characteristics of the champion module based on Me-4PACz+2PACz-K under reverse and forward scan. The active area (AC) and aperture area (AP) are 27 and 29.7 cm^2, respectively. **g** Photos of the module from the front and back side. **h** PCE and FF records for perovskite modules of different area.

Fig. 5. Stability of SAMs and devices. a-b Enlarged ^{1}H-NMR liquid-state spectra of fresh and UV aged **a** Me-4PACz and **b** 2PACz-K. The SAMs in d_6-DMSO are aged under UV light (365 nm, ~1 W cm^{-2}) for 24 h in ambient air. **c-d** The *ab-initio* molecular dynamics (AIMD) structure variation of **c** Me-4PACz and **d** 2PACz-K during the 100 fs trajectories at 5000 K, extracted every 20 fs from the trajectories. **e** KPFM images of fresh ITO/NiO_x/SAM films, and those after DMF washing, heating and UV aging, based on Me-4PACz and Me-4PACz+2PACz-K. All scale bars are 1 μm. **f-g** XRD patterns of perovskite on **f** Me-4PACz and **g** Me-4PACz+2PACz-K after heating at 85 °C. **h** ISOS-L-1 stability protocol under the maximum power point (MPP) tracking conditions under 1-sun equivalent illumination at 25 °C in nitrogen. **i** ISOS-D-2 stability protocol under dark storage in nitrogen at 65 °C.

Fig. 6. Wide-bandgap PSCs and tandem devices. a Chemical structure and IGMH map of 4PADCB and 2PACz-K with isosurface of 0.001 a.u. **b** *J–V* characteristics of the champion 1.78

eV devices under reverse scan. **c** Comparison of PCE for devices of different bandgap in this work. **d-e** 1.78 eV perovskite films aged under 100 mW/cm^2 LED light in ambient air, based on **d** ITO/NiO_x/4PADCB (control) and **e** ITO/NiO_x/4PADCB+2PACz-K (target). **f-g** *In situ* PL mapping evolution of 1.78 eV perovskite films aged under a 20 mW laser in air (25 °C, relative humidity 20%), including **f** PL intensity and **g** wavelength, respectively. All scale bars are 10 μm. **h** *J–V* characteristics of the champion 2T all-perovskite tandem device under reverse and forward scan. **i** EQE spectra of subcells for the best-performing 2T all-perovskite tandem device. **j** PCE records of 2T all-perovskite tandem devices in recent years.

Editorial summary:
Self-assembled monolayers are common hole-selective contacts in inverted perovskite solar cells, but acidic head groups reduce interface quality. Yang et al. neutralize these groups with alkali metal phosphonate salts and mixed layers, improving charge extraction, stability, and efficiency.

Peer review information: *Nature Communications* thanks Xiaojing Hao who co reviewed with Zhen Li; Qingwen Tian, and the other, anonymous, reviewer(s) for their contribution to the peer review of this work. A peer review file is available.

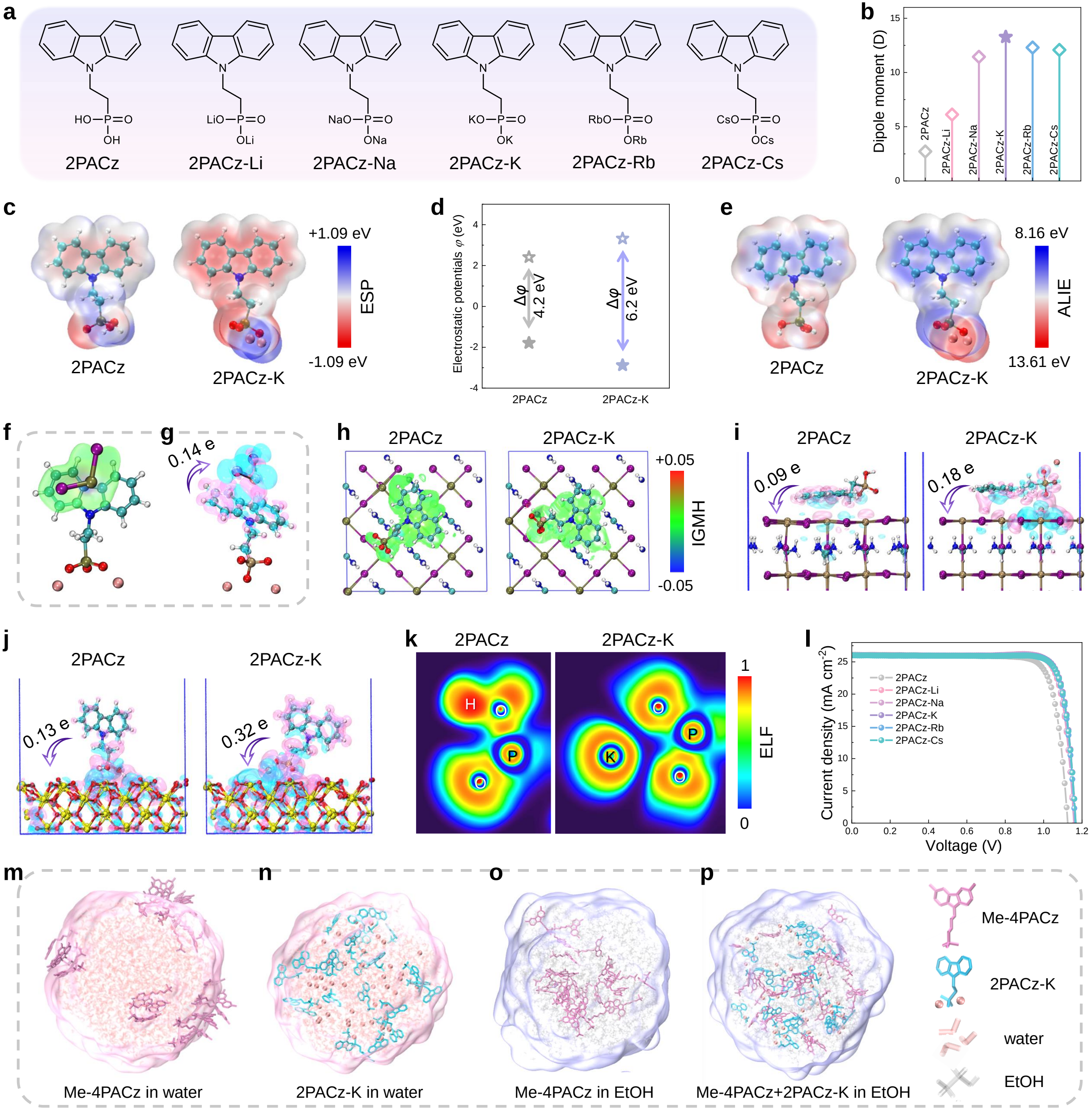
a
HO—P=O
OH
2PACz
LiO—P=O
OLi
2PACz-Li
NaO—P=O
ONa
2PACz-Na
KO—P=O
OK
2PACz-K
RbO—P=O
ORb
2PACz-Rb
CsO—P=O
OCs
2PACz-Cs
b
Dipole moment (D)
2PACz
2PACz-Li
2PACz-Na
2PACz-K
2PACz-Rb
2PACz-Cs
c
+1.09 eV
ESP
-1.09 eV
2PACz
2PACz-K
d
Electrostatic potentials φ (eV)
Δφ 4.2 eV
Δφ 6.2 eV
2PACz
2PACz-K
e
8.16 eV
ALIE
13.61 eV
2PACz
2PACz-K
f
g
0.14 e
h
2PACz
2PACz-K
+0.05
IGMH
-0.05
i
2PACz
2PACz-K
0.09 e
0.18 e
j
2PACz
2PACz-K
0.13 e
0.32 e
k
2PACz
2PACz-K
H
P
K
P
1
ELF
0
l
Current density (mA cm-2)
Voltage (V)
2PACz
2PACz-Li
2PACz-Na
2PACz-K
2PACz-Rb
2PACz-Cs
m
Me-4PACz in water
n
2PACz-K in water
o
Me-4PACz in EtOH
p
Me-4PACz+2PACz-K in EtOH
Me-4PACz
2PACz-K
water
EtOH

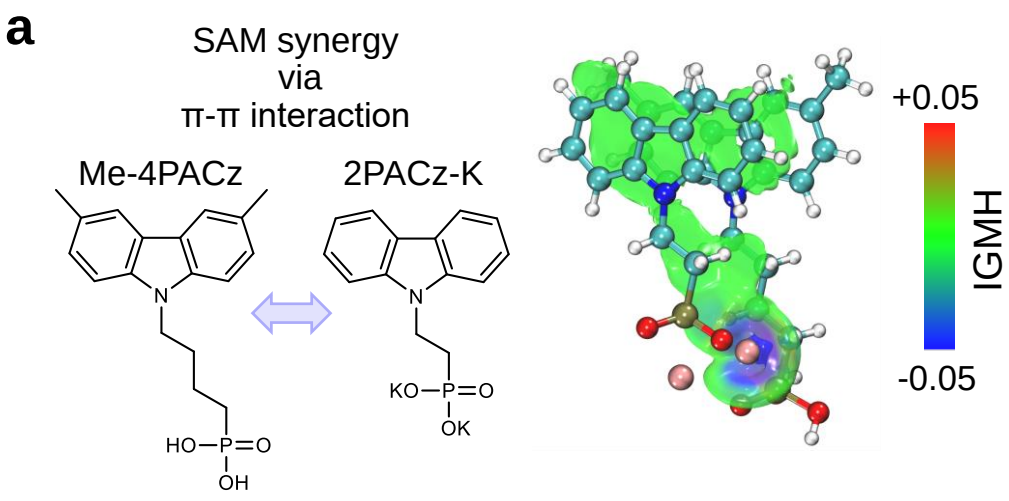
a
SAM synergy
via
π-π interaction
Me-4PACz
2PACz-K
HO—P=O
OH
KO—P=O
OK
N
+0.05
IGMH
-0.05

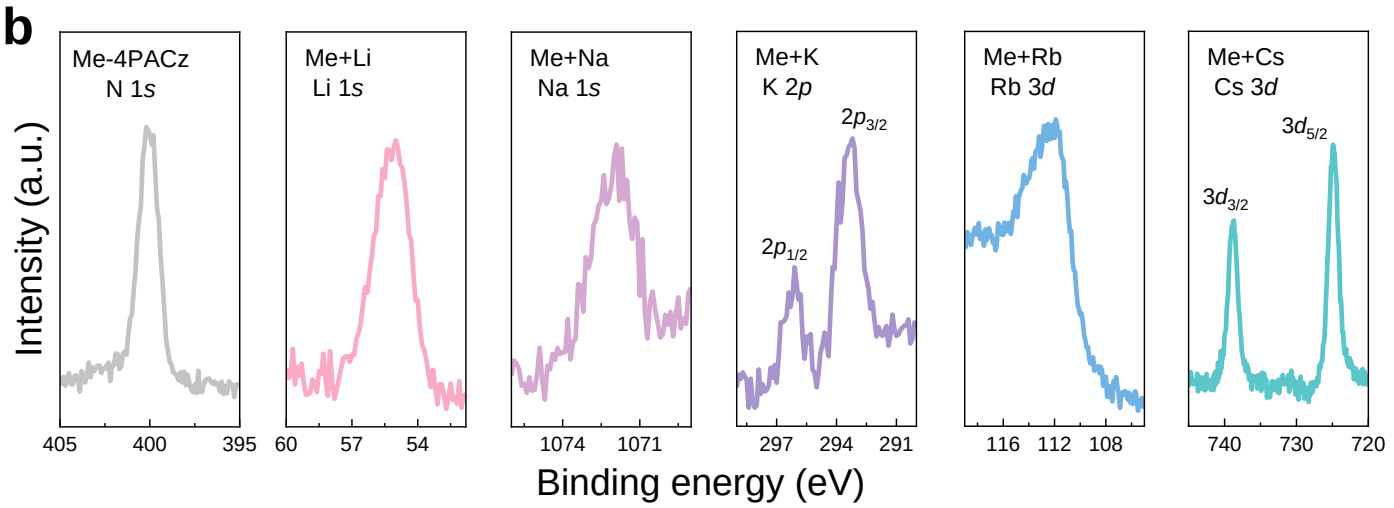
b
Me-4PACz
N 1s
Me+Li
Li 1s
Me+Na
Na 1s
Me+K
K 2p
2p3/2
2p1/2
Me+Rb
Rb 3d
Me+Cs
Cs 3d
3d5/2
3d3/2
Intensity (a.u.)
405
400
395
60
57
54
1074
1071
297
294
291
116
112
108
740
730
720
Binding energy (eV)

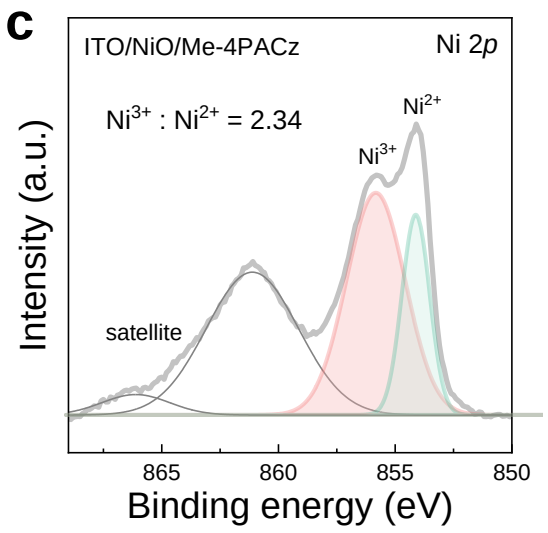
c
ITO/NiO/Me-4PACz
Ni 2p
Ni3+ : Ni2+ = 2.34
Ni2+
Ni3+
satellite
Intensity (a.u.)
865
860
855
850
Binding energy (eV)

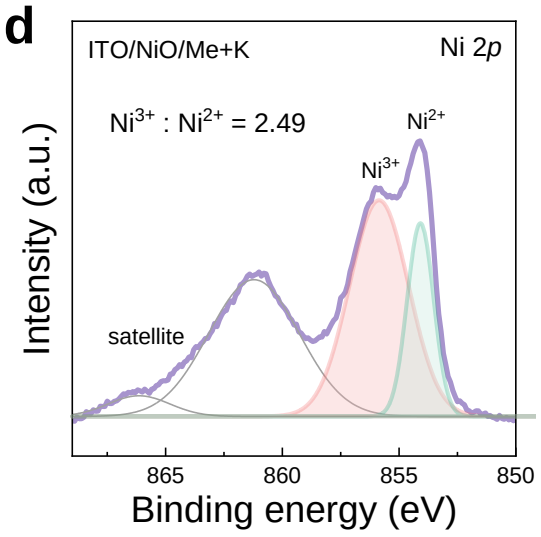
d
ITO/NiO/Me+K
Ni 2p
Ni3+ : Ni2+ = 2.49
Ni2+
Ni3+
satellite
Intensity (a.u.)
865
860
855
850
Binding energy (eV)

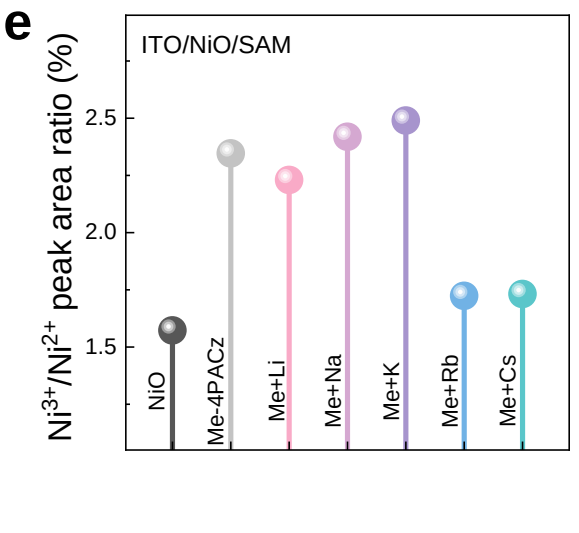
e
ITO/NiO/SAM
Ni3+/Ni2+ peak area ratio (%)
2.5
2.0
1.5
NiO
Me-4PACz
Me+Li
Me+Na
Me+K
Me+Rb
Me+Cs

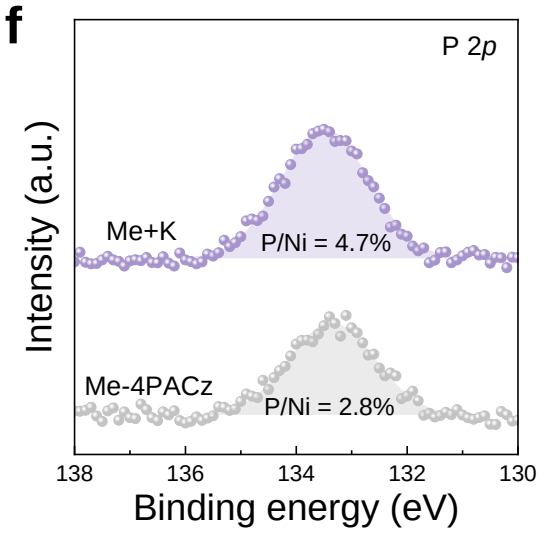
f
P 2p
Me+K
P/Ni = 4.7%
Me-4PACz
P/Ni = 2.8%
Intensity (a.u.)
138
136
134
132
130
Binding energy (eV)

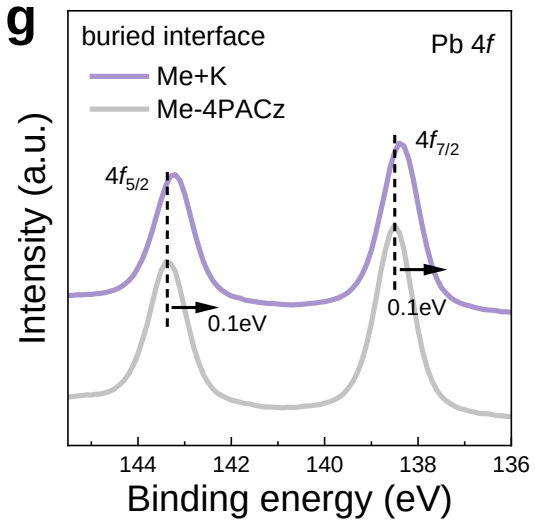
g
buried interface
Pb 4f
Me+K
Me-4PACz
4f5/2
4f7/2
0.1eV
0.1eV
Intensity (a.u.)
144
142
140
138
136
Binding energy (eV)

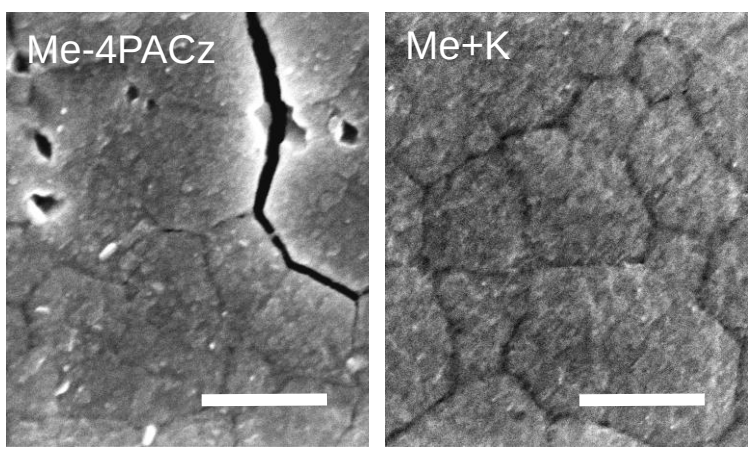
h
Me-4PACz
Me+K

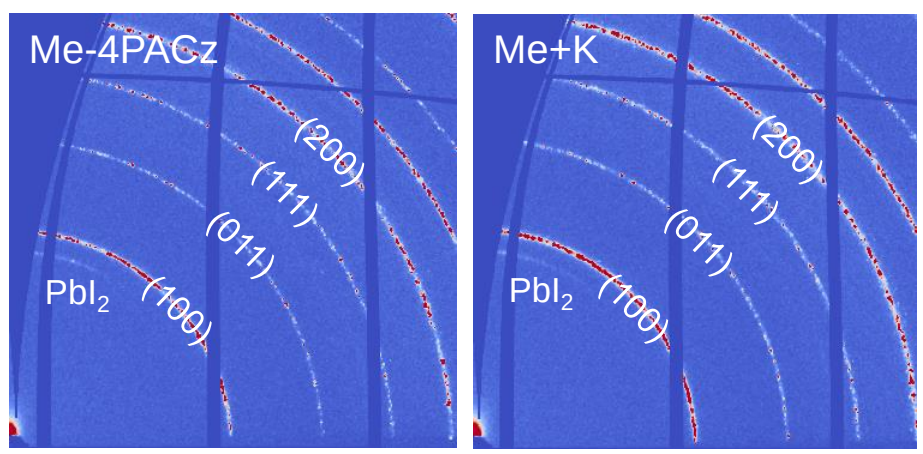
i
Me-4PACz
Me+K
(200)
(111)
(011)
(100)
PbI2

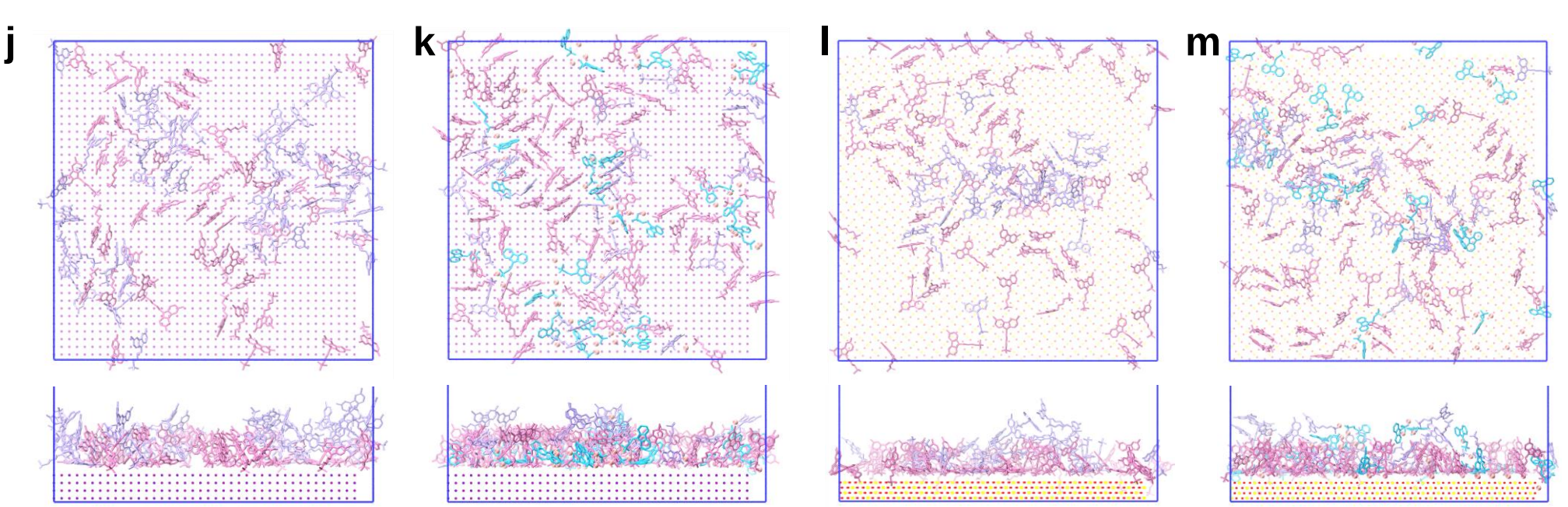
j
k
l
m
adsorbed
Me-4PACz
unadsorbed
Me-4PACz
2PACz-K
NiO substrate
ITO substrate

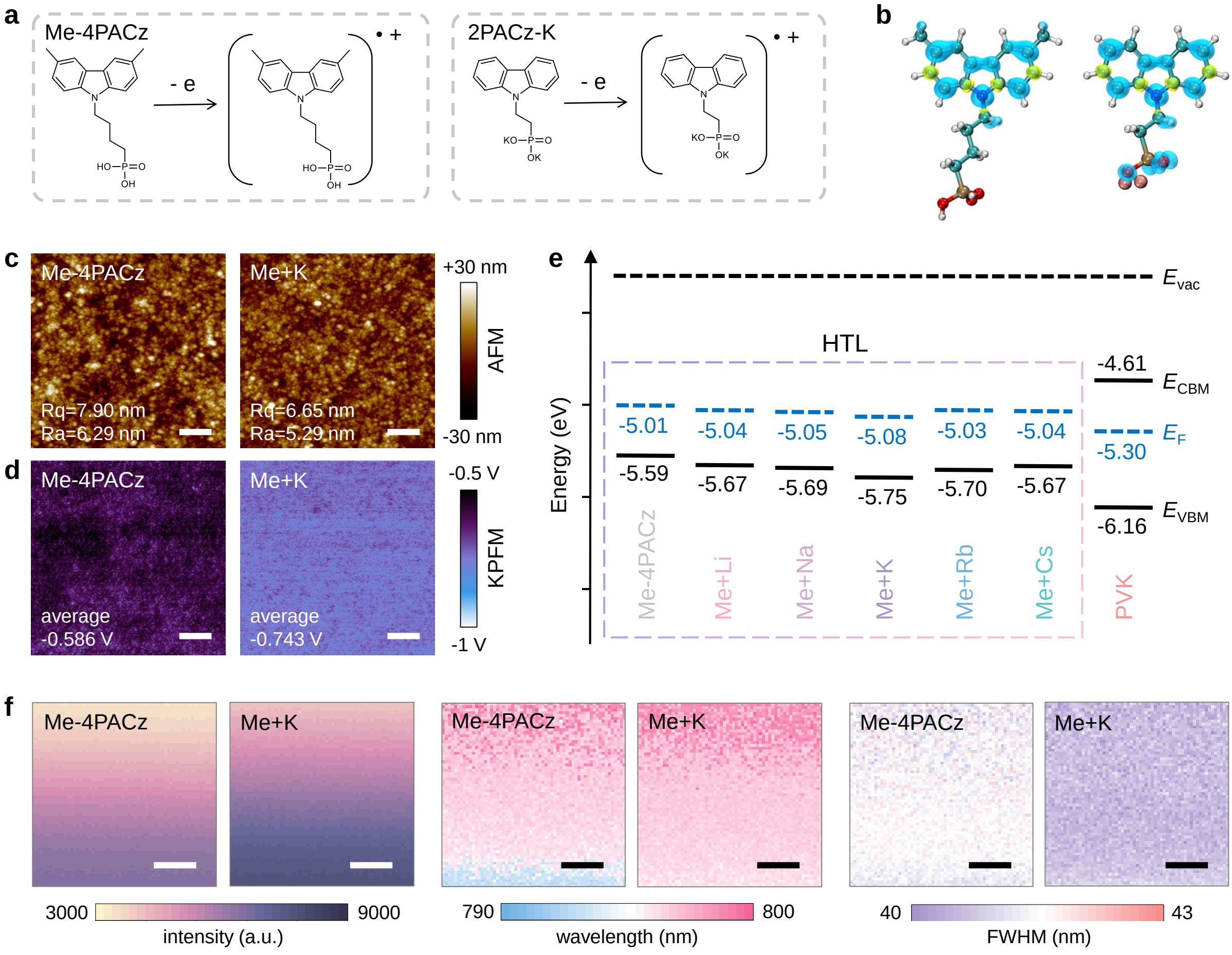
a
Me-4PACz
- e
• +
2PACz-K
- e
• +
b
c
Me-4PACz
Rq=7.90 nm
Ra=6.29 nm
Me+K
Rq=6.65 nm
Ra=5.29 nm
+30 nm
AFM
-30 nm
d
Me-4PACz
average
-0.586 V
Me+K
average
-0.743 V
-0.5 V
KPFM
-1 V
e
E_{vac}
HTL
-4.61
E_{CBM}
-5.01
-5.04
-5.05
-5.08
-5.03
-5.04
E_F
-5.30
-5.59
-5.67
-5.69
-5.75
-5.70
-5.67
E_{VBM}
-6.16
Energy (eV)
Me-4PACz
Me+Li
Me+Na
Me+K
Me+Rb
Me+Cs
PVK
f
Me-4PACz
Me+K
3000
9000
intensity (a.u.)
790
800
wavelength (nm)
40
43
FWHM (nm)

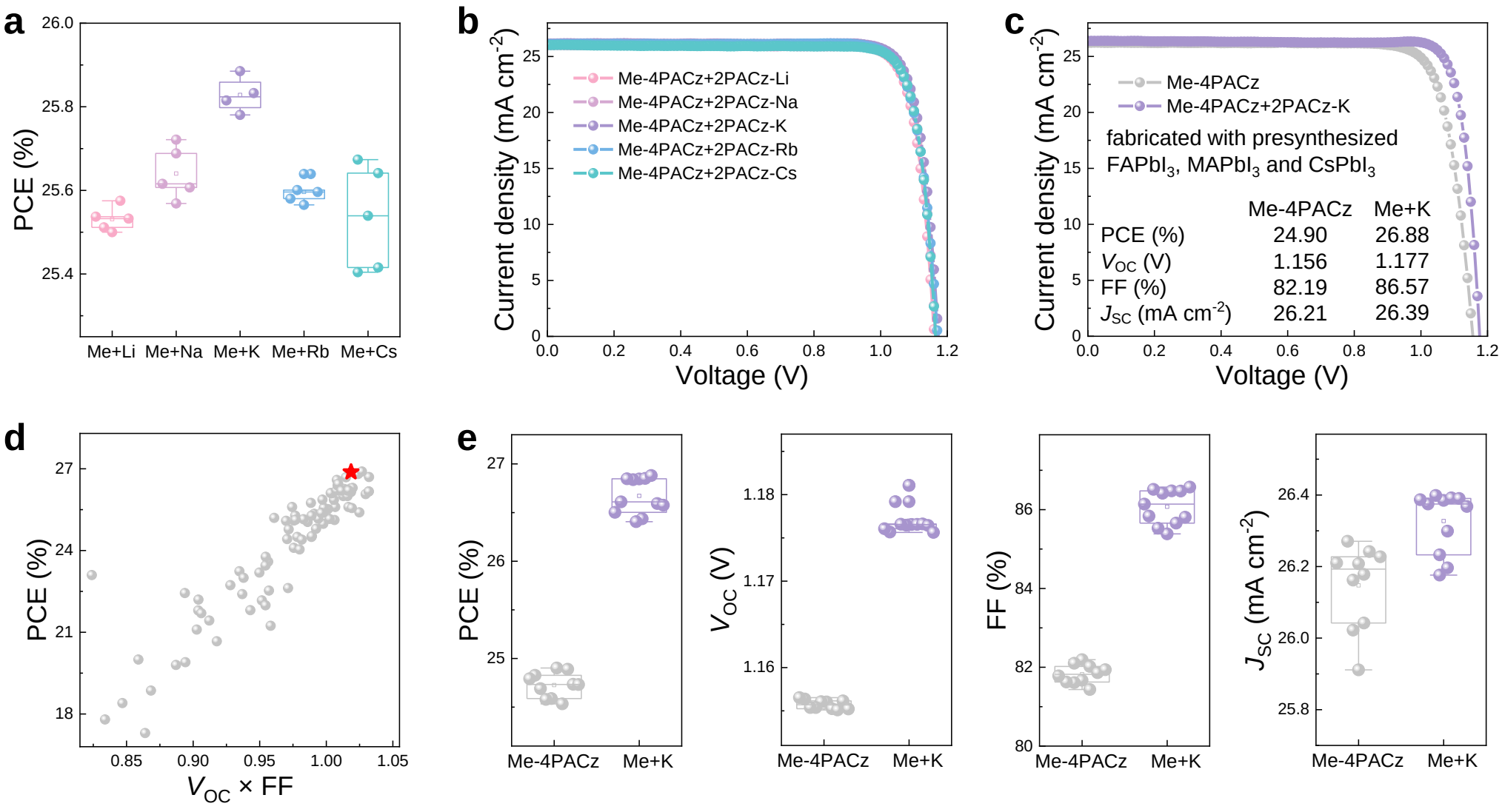
a
PCE (%)
Me+Li
Me+Na
Me+K
Me+Rb
Me+Cs
b
Current density (mA cm-2)
Voltage (V)
Me-4PACz+2PACz-Li
Me-4PACz+2PACz-Na
Me-4PACz+2PACz-K
Me-4PACz+2PACz-Rb
Me-4PACz+2PACz-Cs
c
Me-4PACz
Me-4PACz+2PACz-K
fabricated with presynthesized
FAPbI3, MAPbI3 and CsPbI3
Me-4PACz Me+K
PCE (%) 24.90 26.88
VOC (V) 1.156 1.177
FF (%) 82.19 86.57
JSC (mA cm-2) 26.21 26.39
d
PCE (%)
VOC × FF
e
PCE (%)
VOC (V)
FF (%)
JSC (mA cm-2)
Me-4PACz
Me+K

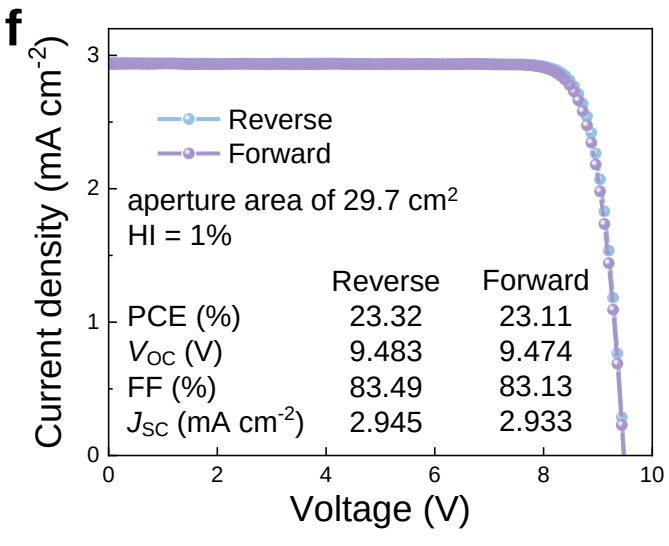
f
Current density (mA cm-2)
Voltage (V)
Reverse
Forward
aperture area of 29.7 cm2
HI = 1%
Reverse Forward
PCE (%) 23.32 23.11
VOC (V) 9.483 9.474
FF (%) 83.49 83.13
JSC (mA cm-2) 2.945 2.933

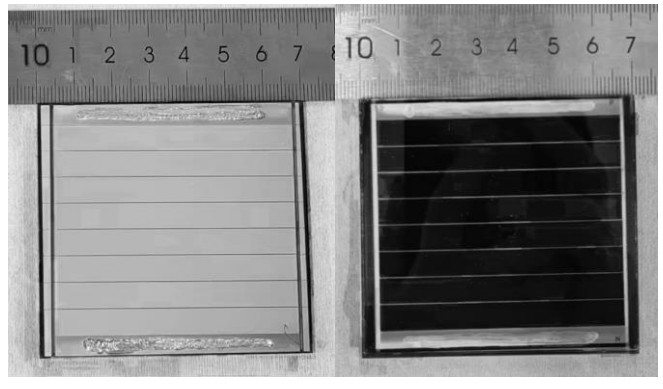

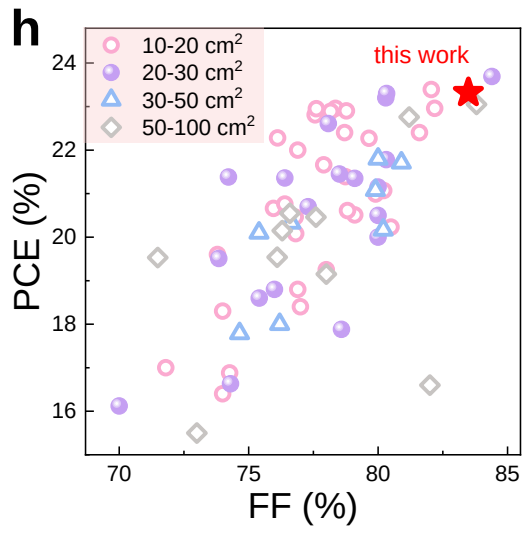
h
10-20 cm2
20-30 cm2
30-50 cm2
50-100 cm2
this work
PCE (%)
FF (%)

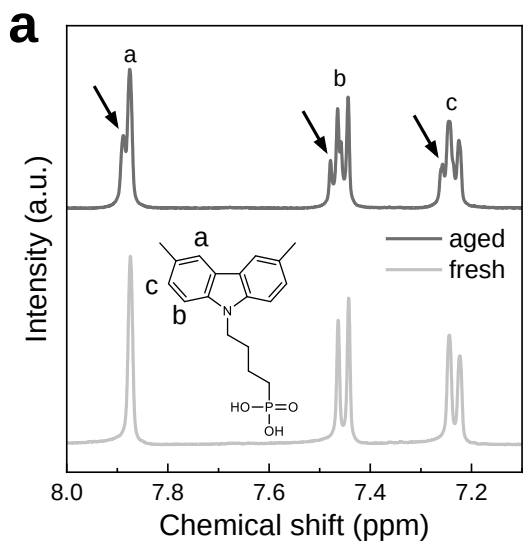
a
Intensity (a.u.)
a
b
c
aged
fresh
HO—P=O
OH
8.0
7.8
7.6
7.4
7.2
Chemical shift (ppm)

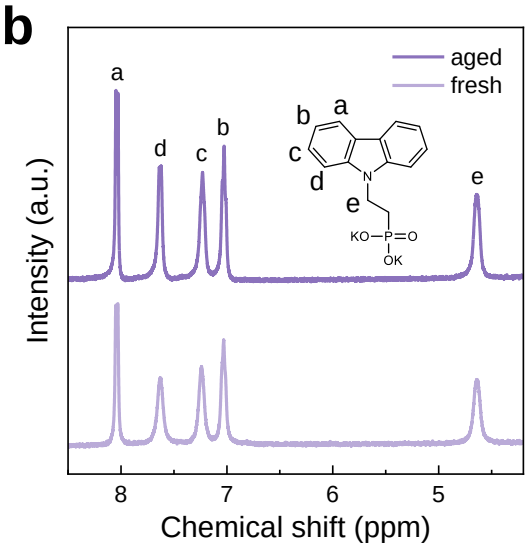
b
Intensity (a.u.)
aged
fresh
a
d
c
b
e
KO—P=O
OK
8
7
6
5
Chemical shift (ppm)

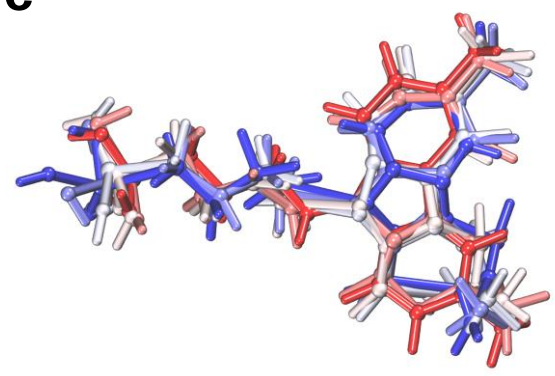
c
Me-4PACz

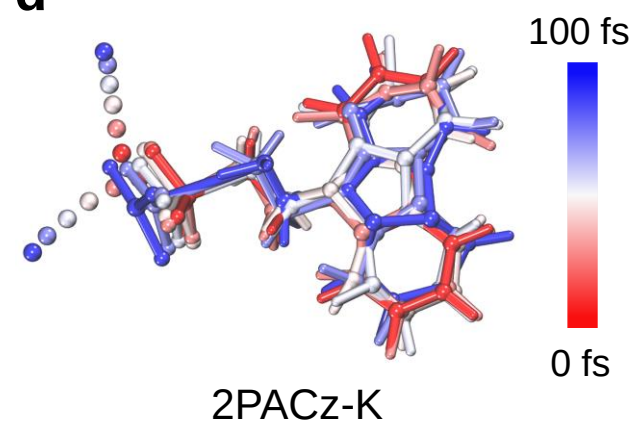
d
100 fs
0 fs
2PACz-K

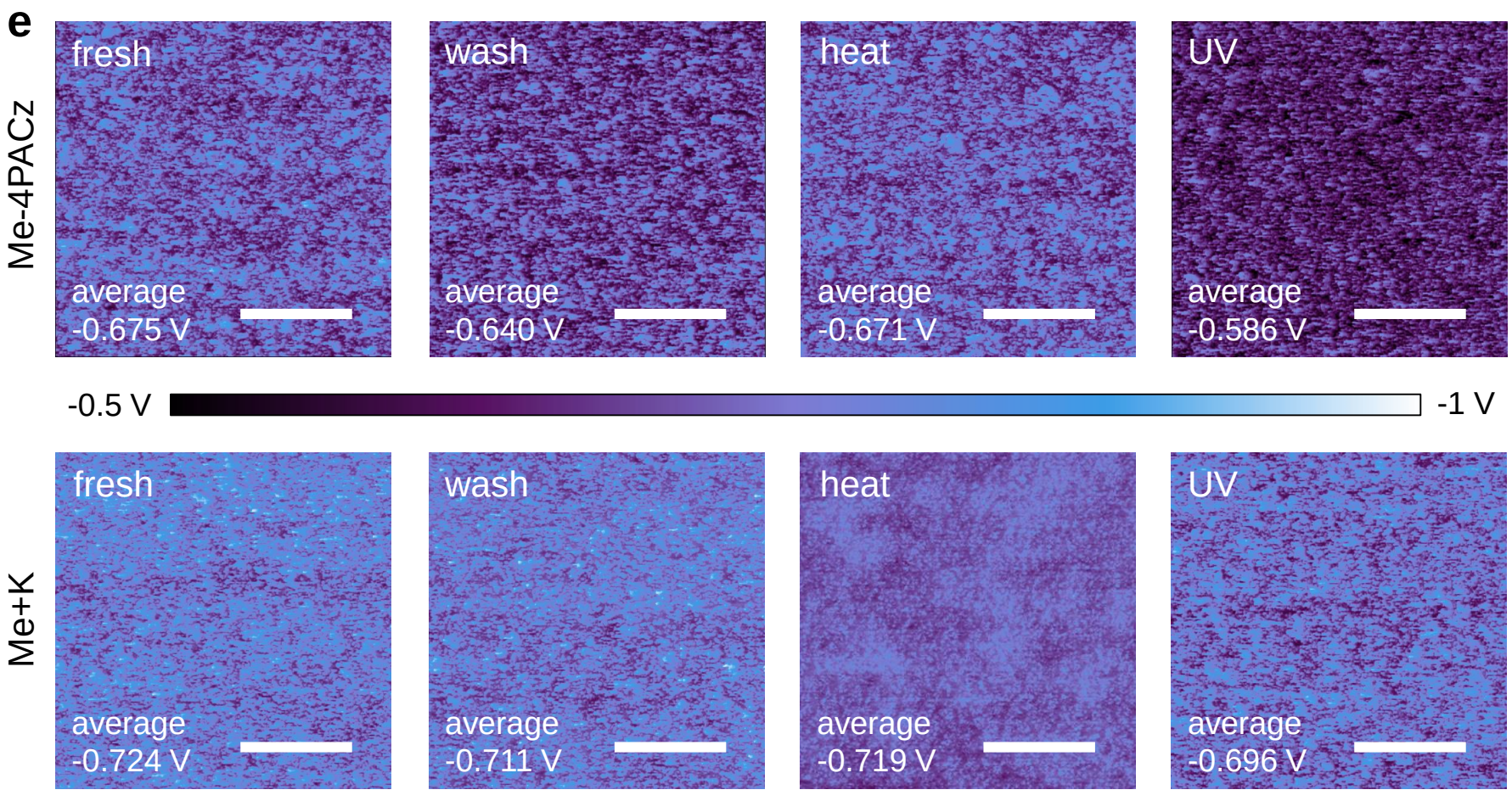
e
Me-4PACz
fresh
average
-0.675 V
wash
average
-0.640 V
heat
average
-0.671 V
UV
average
-0.586 V
-0.5 V
-1 V
Me+K
fresh
average
-0.724 V
wash
average
-0.711 V
heat
average
-0.719 V
UV
average
-0.696 V

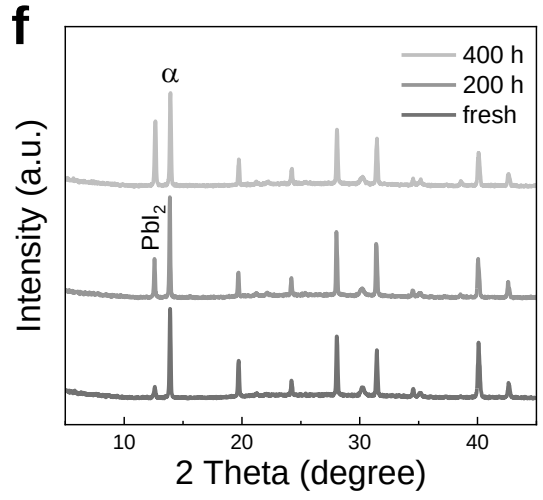
f
Intensity (a.u.)
α
PbI2
400 h
200 h
fresh
10
20
30
40
2 Theta (degree)

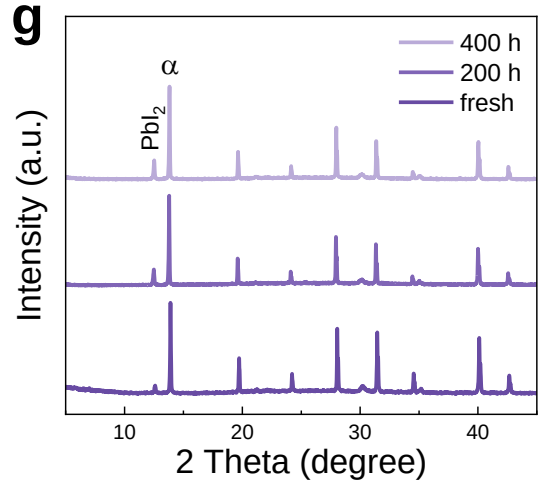
g
Intensity (a.u.)
α
PbI2
400 h
200 h
fresh
10
20
30
40
2 Theta (degree)

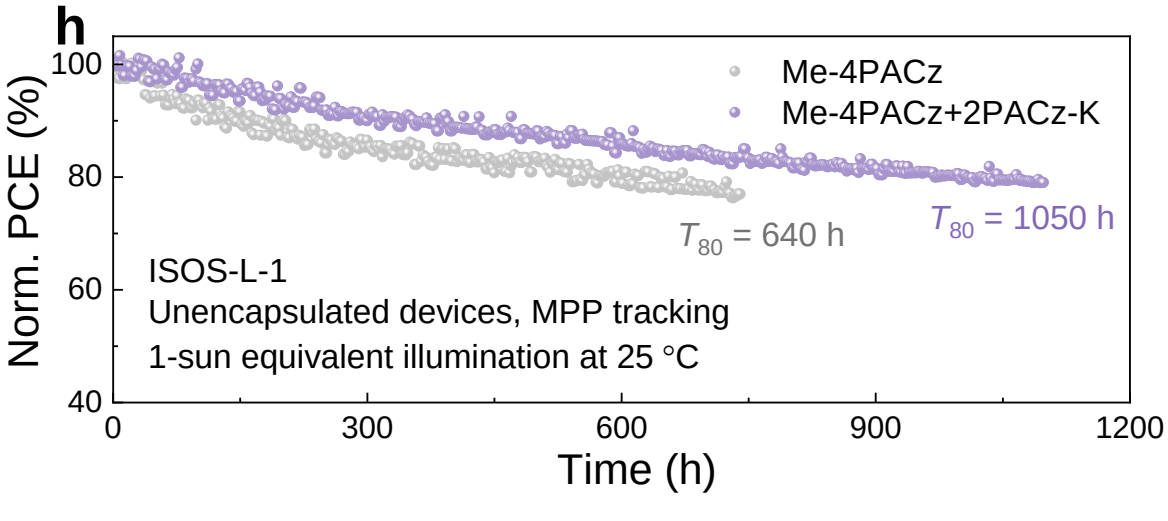
h
Norm. PCE (%)
100
80
60
40
Me-4PACz
Me-4PACz+2PACz-K
T80 = 640 h
T80 = 1050 h
ISOS-L-1
Unencapsulated devices, MPP tracking
1-sun equivalent illumination at 25 °C
0
300
600
900
1200
Time (h)

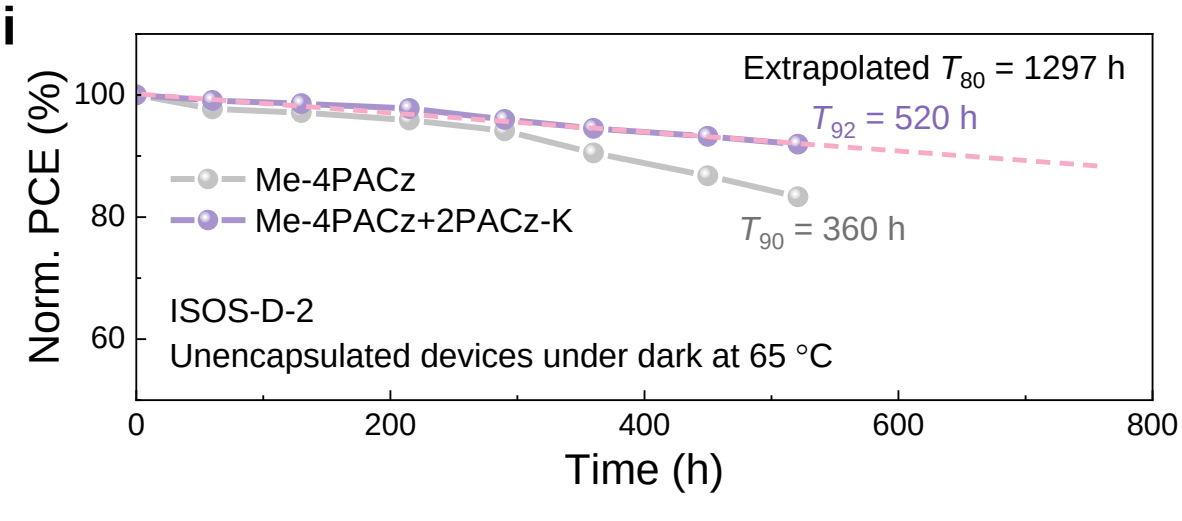
i
Norm. PCE (%)
100
80
60
Extrapolated T80 = 1297 h
T92 = 520 h
Me-4PACz
Me-4PACz+2PACz-K
T90 = 360 h
ISOS-D-2
Unencapsulated devices under dark at 65 °C
0
200
400
600
800
Time (h)

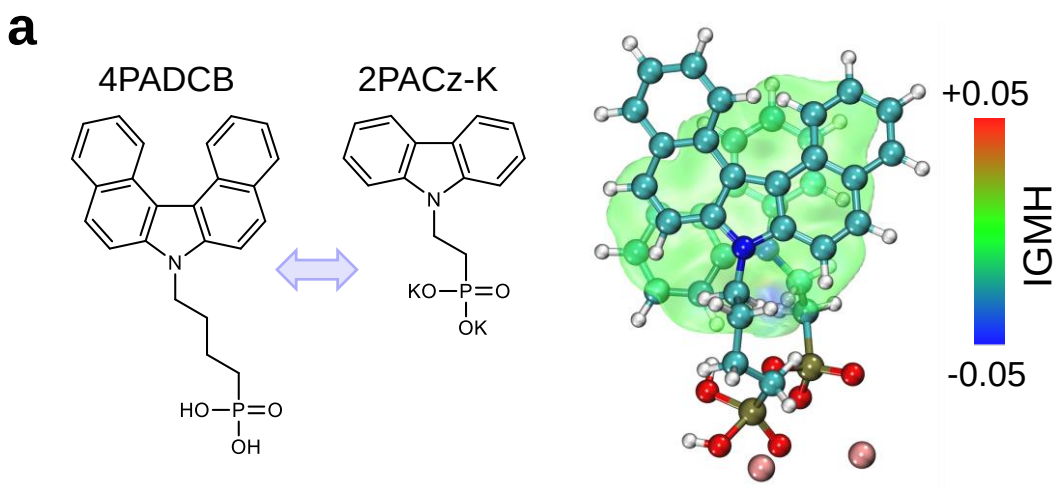
a
4PADCB
2PACz-K
HO—P=O
OH
KO—P=O
OK
+0.05
IGMH
-0.05

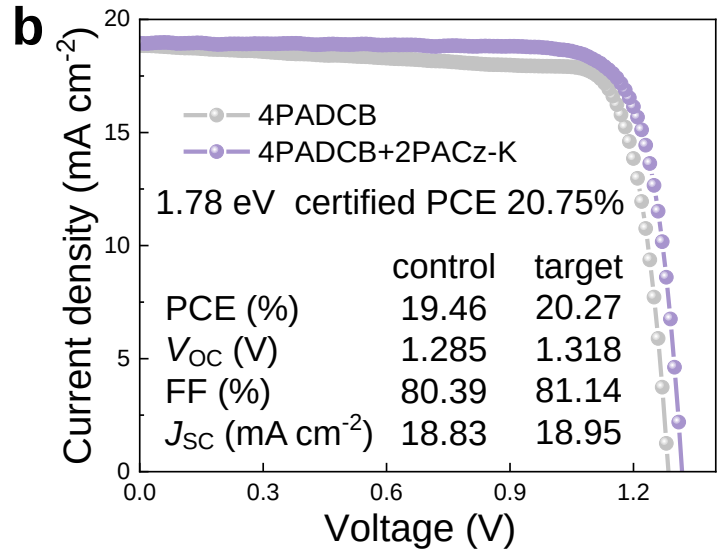
b
Current density (mA cm-2)
Voltage (V)
4PADCB
4PADCB+2PACz-K
1.78 eV certified PCE 20.75%
control target
PCE (%) 19.46 20.27
VOC (V) 1.285 1.318
FF (%) 80.39 81.14
JSC (mA cm-2) 18.83 18.95

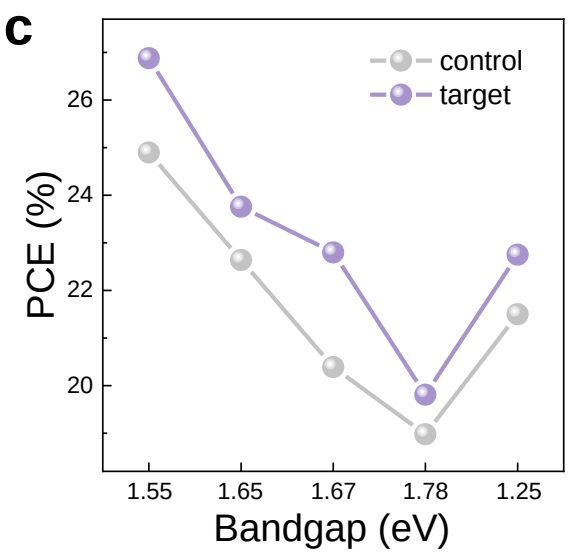
c
PCE (%)
Bandgap (eV)
control
target

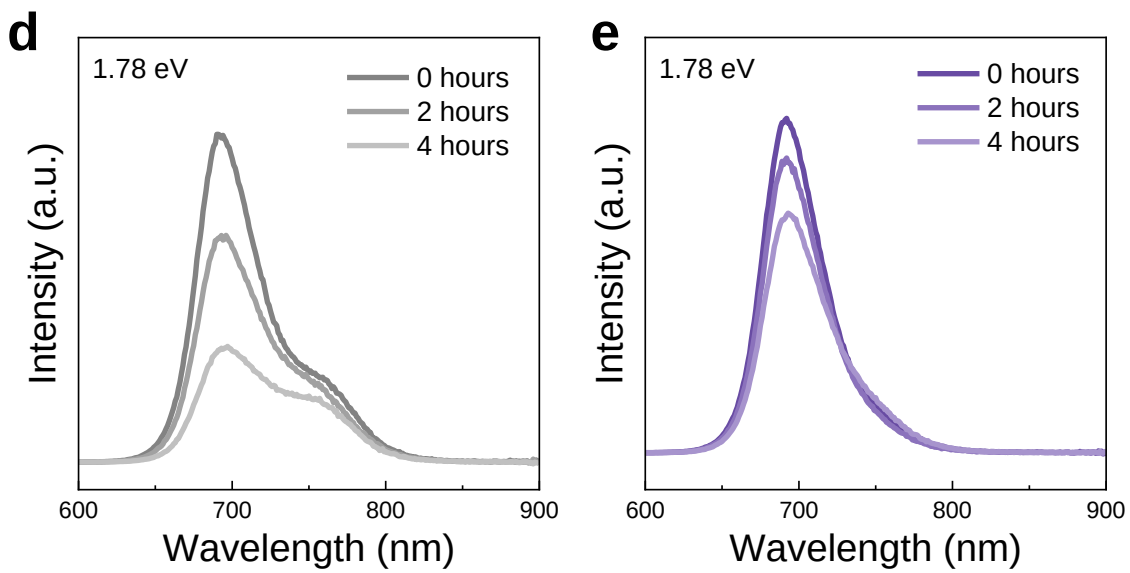
d
1.78 eV
0 hours
2 hours
4 hours
Intensity (a.u.)
Wavelength (nm)

e
1.78 eV
0 hours
2 hours
4 hours
Intensity (a.u.)
Wavelength (nm)

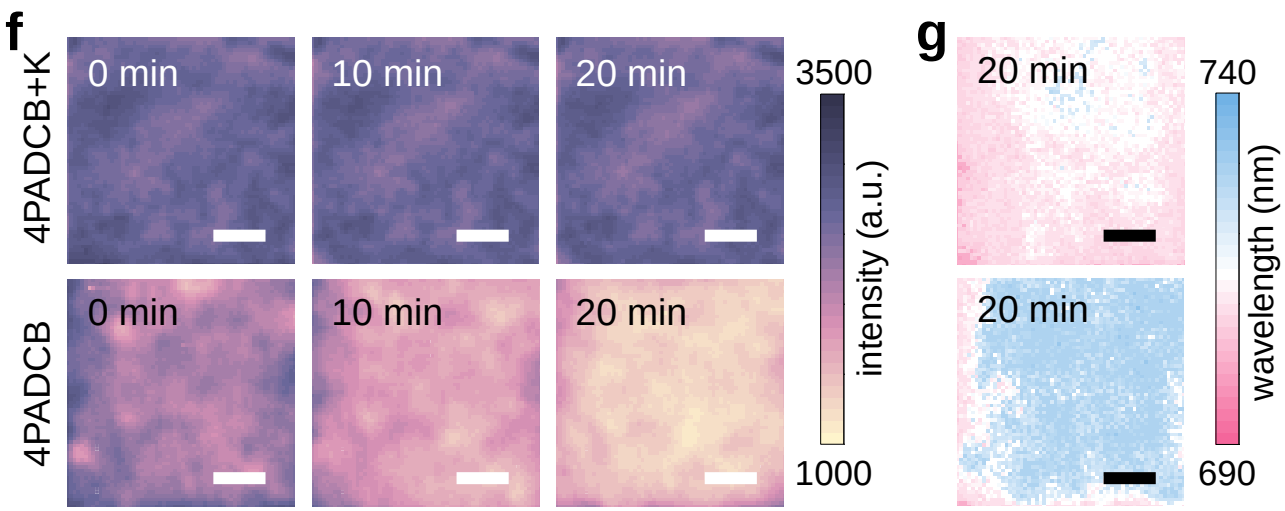
f
4PADCB+K
4PADCB
0 min
10 min
20 min
3500
1000
intensity (a.u.)
g
20 min
740
690
wavelength (nm)

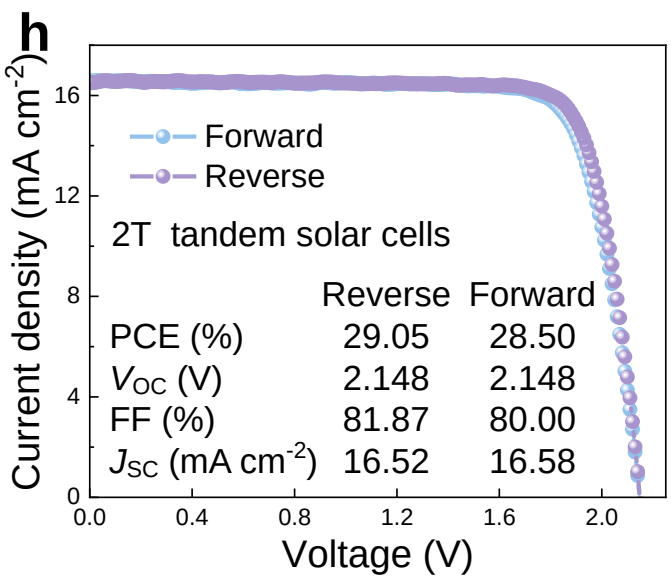
h
Current density (mA cm-2)
Voltage (V)
Forward
Reverse
2T tandem solar cells
Reverse Forward
PCE (%) 29.05 28.50
VOC (V) 2.148 2.148
FF (%) 81.87 80.00
JSC (mA cm-2) 16.52 16.58

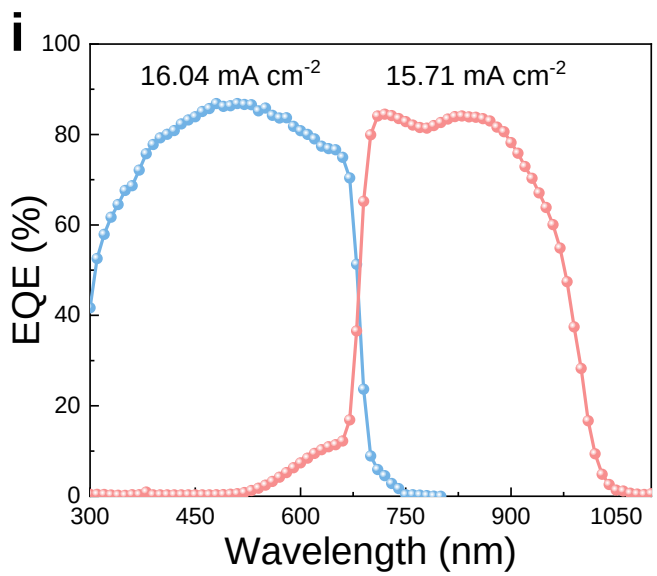
i
16.04 mA cm-2
15.71 mA cm-2
EQE (%)
Wavelength (nm)

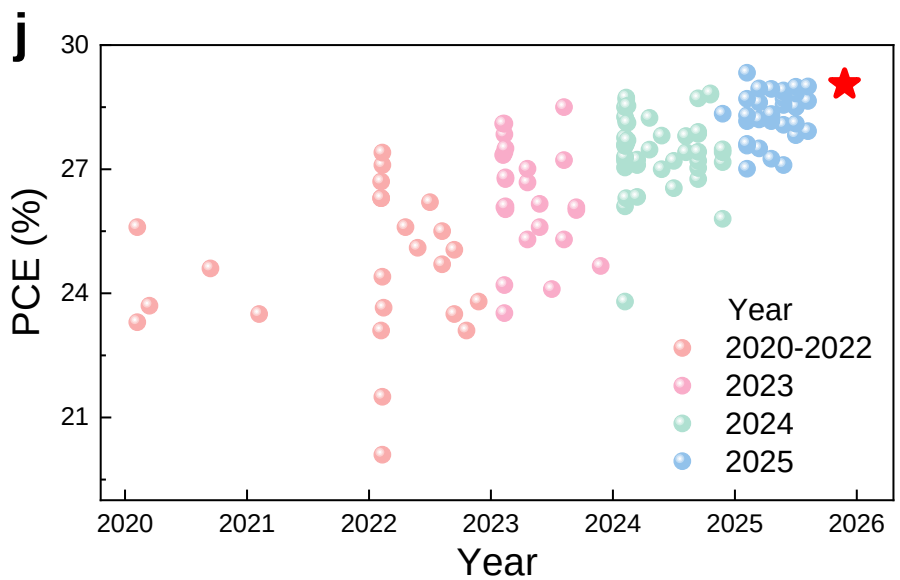
j
PCE (%)
Year
Year
2020-2022
2023
2024
2025